iScience

CellPress

Article

Utilizing Polymer Micelle to Control Dye J-aggregation and Enhance Its Theranostic Capability

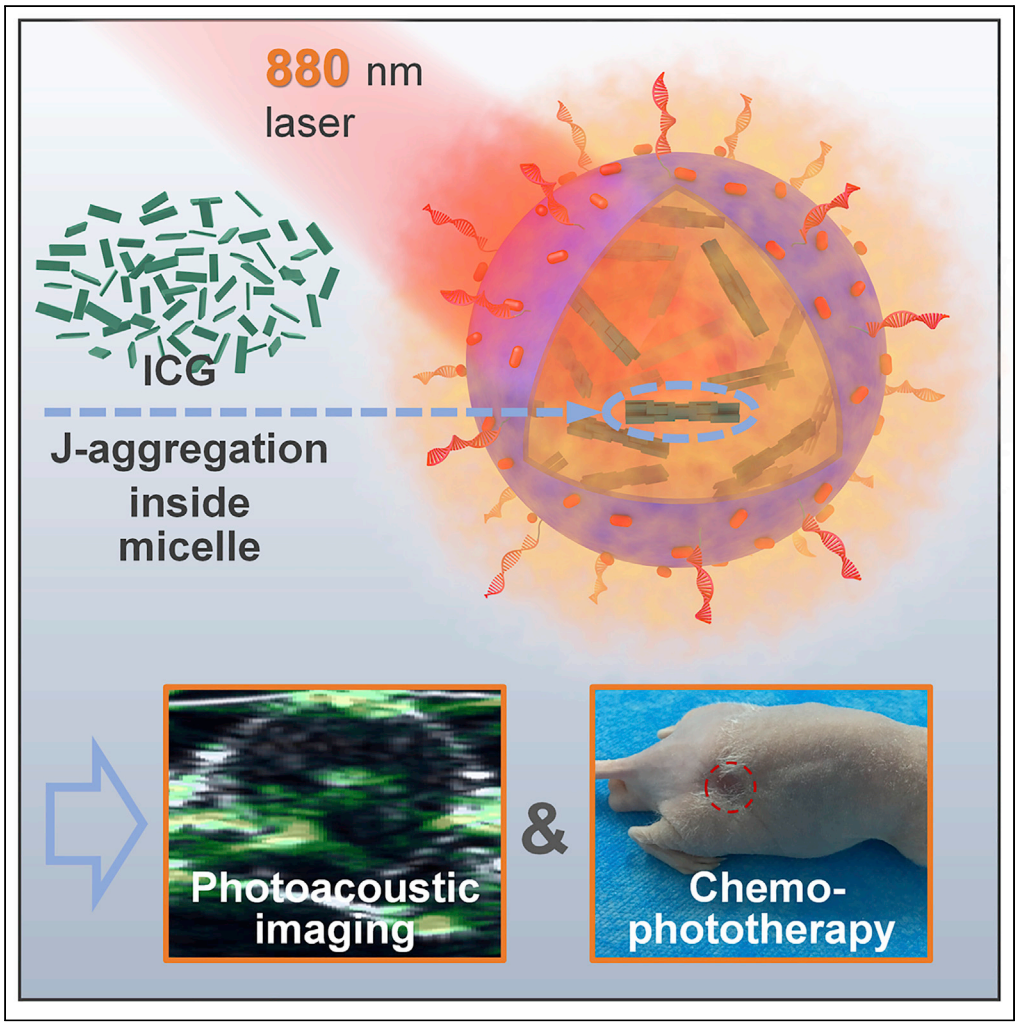

Chen Shao, Fan Xiao, Heng Guo, ..., Changfeng Wu, Lei Xi, Leilei Tian

xilei@sustech.edu.cn (L.X.)
tianll@sustech.edu.cn (L.T.)

HIGHLIGHTS

J-aggregation of ICG is facilitated by polymer micelle

Proper host-guest interactions are very critical

The aggregation significantly improves the capability of ICG in phototheranostics

The hierarchical assembly exhibits excellent photo/bio-stability

Shao et al., iScience *22*, 229–239
December 20, 2019
https://doi.org/10.1016/j.isci.2019.11.022

iScience

CellPress

Article

Utilizing Polymer Micelle to Control Dye J-aggregation and Enhance Its Theranostic Capability

Chen Shao,[1] Fan Xiao,[1] Heng Guo,[2] Jiantao Yu,[1] Dong Jin,[1] Changfeng Wu,[2] Lei Xi,[2,*] and Leilei Tian[1,3,*]

SUMMARY

We utilize polymer micelle to precisely control indocyanine green (ICG) J-aggregation in a fast and highly efficient way. In addition to simple encapsulation, the polymer micelle plays a role as a host template to drive ICG J-aggregation by the synergy of electrostatic and hydrophobic attractions. We further demonstrate that, due to the robust host-guest interaction, the intact of ICG J-aggregate will be secured by the polymer encapsulation during the intracellular and *in vivo* incubation. These features make this hierarchical assembly between ICG J-aggregate and the micelle polymer a promising biomedicine for cancer phototheranostics. Therefore the complex micelles are further modified by introduction of doxorubicin for chemotherapy and DNA aptamer for tumor targeting, and the final multi-functional micellar medicine shows high therapeutic efficacy for tumor, i.e., the tumor can be completely eliminated with no local reoccurrence and without long-term toxicity or side effects during a 24-day period after the treatment.

INTRODUCTION

Nature has created remarkable examples of dye assembly that are vital for sustaining life. For instance, the formation of chlorophyll J-aggregates can afford intense near-infrared (NIR) absorption up to ~900 nm, which enables the more efficient light harvesting of sunlight (Sengupta and Würthner, 2013). Organic biomedical materials have been quickly developed in recent years because of their biodegradability, robust biocompatibility, and long-term biological safety (Song et al., 2015a, 2015b; Pu et al., 2014; Qi et al., 2017; Zheng et al., 2013). During the process, the supramolecular strategy plays an increasingly important role as weak noncovalent interactions will influence the properties of organic biomedicines by controlling the molecular packing structure and self-assembly morphology (Gorl et al., 2012; Yin et al., 2019; Varughese, 2014; Su et al., 2019; Cai et al., 2018a, 2018b, 2018c). For instance, Zheng and co-workers developed porphyrin-lipid conjugates, which self-assembled into porphysome. Although porphyrin has been extensively investigated in biomedical applications, the porphysome shows distinguished optical properties with improved performance in photothermal therapy (PTT) and photoacoustic imaging (PAI) (Lovell et al., 2011). In another example, supramolecular complex between cucurbit[7]uril and organic conjugated radical was developed by Zhang and co-workers; the organic radical itself suffers from radical annihilation caused by π-π stacking and its NIR absorption would be impaired. Accordingly, in addition to functioning as a drug delivery vehicle, the macrocycle acted as a shield to preserve the organic radical and its absorption, finally making the complex applicable in PTT (Jiao et al., 2015).

The NIR cyanine dyes with long-wavelength absorption and high extinction coefficient show great potential in phototheranostics nowadays (Luo et al., 2011; Porcu et al., 2016; Guo et al., 2014). However, as they are vulnerable to photo-irradiation and the complex biological environment (Cai et al., 2018a, 2018b, 2018c; Sheng et al., 2013), cyanine dyes are generally complexed with other materials for practical applications, and polymer encapsulation is one of the approaches (Zheng et al., 2013; Song et al., 2014, 2015a, 2015b). Herein, we report an example of advanced supramolecular medicine between amphiphilic polymer DSPE-PEG_{2k}-NH_2 and indocyanine green (ICG), a representative cyanine dye, in which the beneficial interactions between the polymer carrier and dye bring superior properties to the complex system (Scheme 1). Rather than a simple encapsulation, these polymer micelles can induce the guest ICG molecules to a complete J-aggregation and enhance their optical properties for phototheranostic applications, i.e., the micelle-encapsulated ICG J-aggregate showed a deeper NIR absorption (a redshift from 780 to 895 nm) with a higher absorption coefficient (78.0 $L \cdot g^{-1} \cdot cm^{-1}$ versus 45.0 $L \cdot g^{-1} \cdot cm^{-1}$ of free ICG), higher

[1]Department of Materials Science and Engineering, Southern University of Science and Technology, 1088 Xueyuan Boulevard, Shenzhen, Guangdong 518055, P. R. China

[2]Department of Biomedical Engineering, Southern University of Science and Technology, 1088 Xueyuan Boulevard, Shenzhen, Guangdong 518055, P. R. China

[3]Lead Contact

*Correspondence: xilei@sustech.edu.cn (L.X.), tianll@sustech.edu.cn (L.T.)

https://doi.org/10.1016/j.isci.2019.11.022

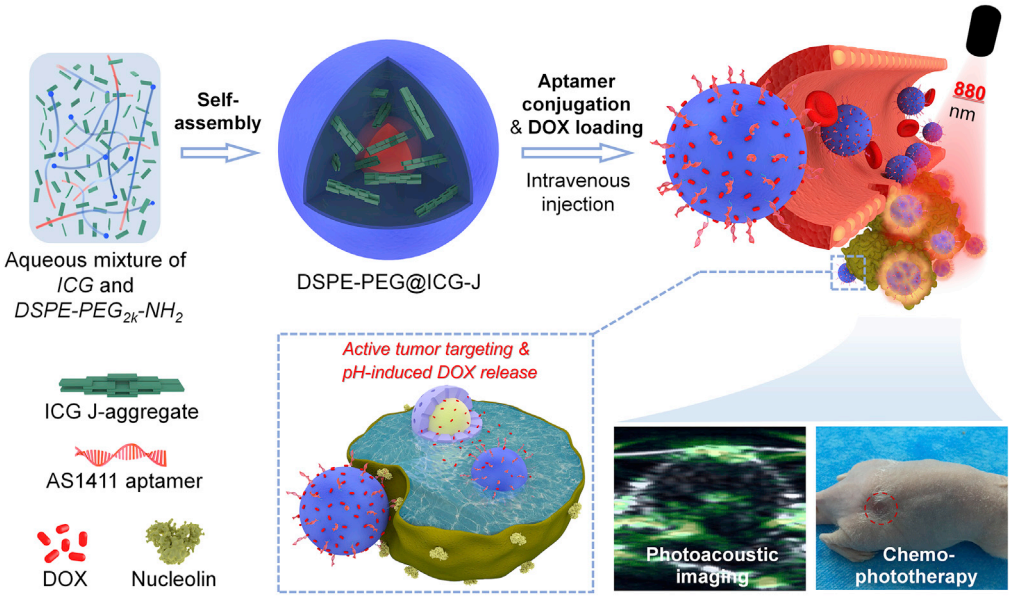

Scheme 1. Illustration of the Formation of the Supramolecular Medicine Based on Polymer Micelle and ICG J-aggregate and Its Application in PAI-Guided Chemo-phototherapy

See also Table S1.

penetration capability, and enhanced photothermal effect and photostability. Recently, the construction of aggregates by noncovalent interaction has been proved to be an effective strategy to improve the function and stability of organic dyes (Song et al., 2016; Gaufres et al., 2014; Eisele et al., 2012). Moreover, compared with random aggregation, dye J-aggregate with regular head-to-tail molecular packing featuring a deeper and stronger absorption (Coles et al., 2010) has attracted extensive attentions (Wurthner et al., 2011; Cai et al., 2018a, 2018b, 2018c; Kim et al., 2018; Walker et al., 2011; He et al., 2017; Chen et al., 2017; Zhao et al., 2008; Horn and Rieger, 2001; Huang et al., 2015). However, the formation of dye J-aggregate and the subsequent biomedical application are challenging, which requires a long formation time at a high concentration and lacks structural stability for *in vivo* application (Liu et al., 2017; von Berlepsch et al., 2007; Egawa et al., 2007; von Berlepsch and Bottcher, 2010). In the system that we explored in this article, facilitated by the host-guest interactions of polymer micelles, the ICG molecules in dilute solution can convert to complete J-aggregate within 8 h. What's more, the ICG J-aggregate in the supramolecular assembly showed robust stability under intracellular and *in vivo* incubation, making this material more accessible to biomedical applications. To the best of our knowledge, there is rare report on the precise control of dye aggregation by adjusting the host-guest interactions between the polymer carrier and the encapsulated dye. As another benefit of micelle encapsulation, the as-fabricated complex micelle can be functionalized conveniently. In this work, to reach a better therapeutic effect, the negative charge and functional groups of the complex micelle with ICG J-aggregate in encapsulation were employed to introduce doxorubicin (DOX) through electrostatic interaction for chemotherapy and to covalently conjugate DNA aptamer for active tumor targeting (Scheme 1). The *in vivo* anticancer experiment proved that the final multi-functional micellar medicine, which combined J-aggregation-enhanced PTT, aptamer targeting and enhanced permeability and retention (EPR)-promoted tumor enrichment, and chemotherapy based on DOX sustained release, accomplished complete tumor elimination with no local reoccurrence within 24 days. Last but not the least, in addition to the superior therapeutic performance, this micellar medicine showed reliable biocompatibility without long-term toxicity and side effects.

RESULTS AND DISCUSSION

Fabrication and Characterization of DSPE-PEG@ICG-J

ICG aqueous solution showed two absorption peaks at 715 and 780 nm from its monomer and dimer, respectively. Occasionally, we observed an interesting phenomenon that, after being co-dissolved with phospholipid-poly(ethylene glycol), DSPE-PEG_{2k}-NH_2, in ultrapure water and stirred at room temperature

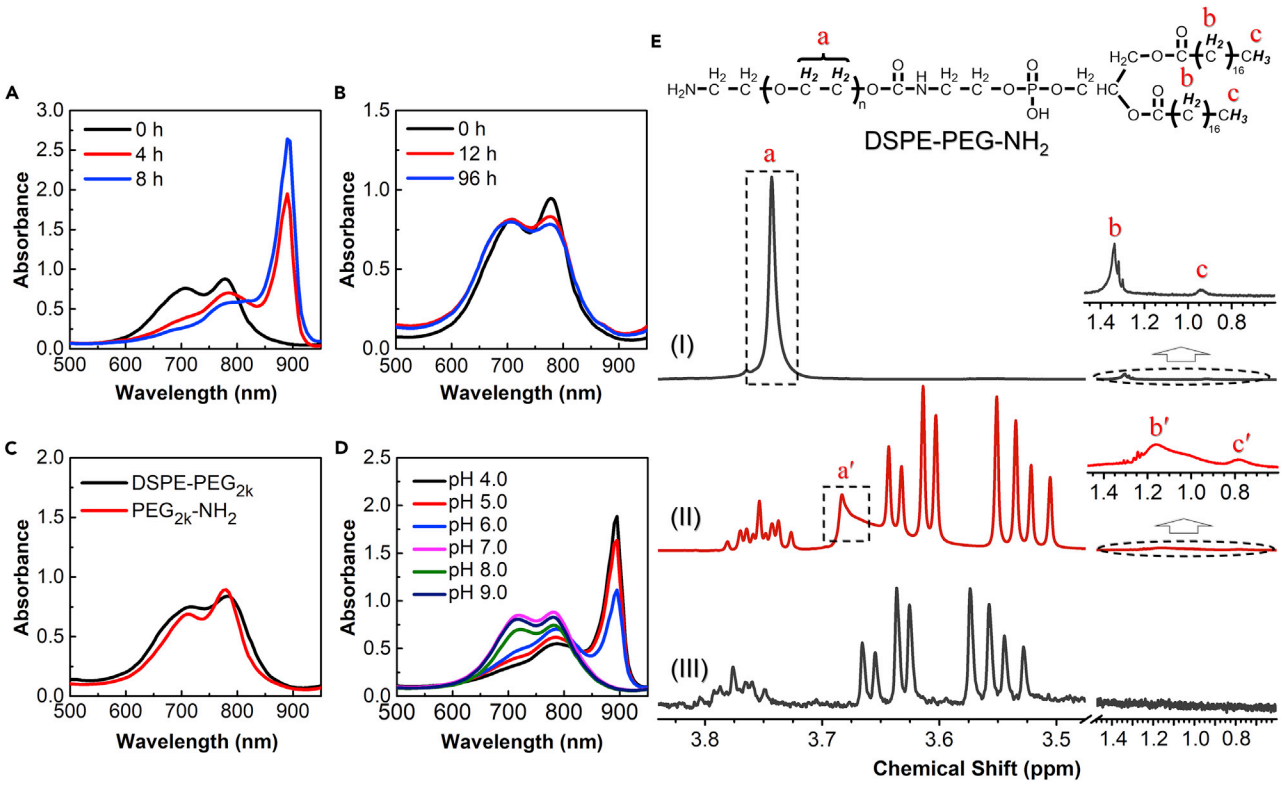

Figure 1. ICG J-aggregation under Different Conditions and ^{1}H NMR Characterization

(A–E) Monitoring ICG J-aggregation (A) in the presence of DSPE-PEG_{2k}-NH_2 (0.2 mg·mL^{-1}) with a 15-min 80°C heating before room temperature stirring in water, (B) in the absence of additive with room temperature stirring in water, (C) in the presence of DSPE-PEG_{2k} or PEG_{2k}-NH_2 (0.2 mg·mL^{-1}) with a 24-h room temperature stirring in water, and (D) in the presence of DSPE-PEG_{2k}-NH_2 (0.2 mg·mL^{-1}) with room temperature stirring in buffers with various pH values. In these experiments, the concentration of ICG was 50.0 μg·mL^{-1}. (E) ^{1}H NMR spectra of (I) DSPE-PEG_{2k}-NH_2 micelle, (II) DSPE-PEG_{2k}-NH_2 micelle with ICG J-aggregate in encapsulation, and (III) naked ICG J-aggregate. See also Figures S1–S3.

for 8 h, ICG showed significantly changed absorption with a shaper and red-shifted peak at 895 nm (Figures 1A and S1A), which indicates the formation of ICG J-aggregate (Liu et al., 2017). However, without the presence of the micelle polymer, ICG under the same concentration (50 μg·mL^{-1}) did not convert to J-aggregate at all, even after a long incubation of 96 h (Figure 1B), implying the important role of the micelle polymer. In the further study, we observed that ICG J-aggregate did not form with DSPE-PEG polymer without the amine functionalization (Figures 1C and S1B). It indicated that the positive charge of amine groups probably played an important role. Therefore, we modulated the charge of amine groups by adjusting the pH value. As shown in Figure 1D, under neutral or alkaline conditions, no ICG J-aggregate formed after an 8-h incubation at room temperature; on the contrary, the majority of free ICG converted to J-aggregate under acidic conditions, and the more acidic the buffer was, the higher the conversion yield achieved. All the results demonstrated that the electrostatic interaction between the positive charge of amine groups and the negatively charged ICG probably is critical for ICG J-aggregation.

In addition to the electrostatic interaction, the role of micellar structure formed by DSPE-PEG_{2k}-NH_2 was studied. As a control experiment, PEG_{2k}-NH_2 (both at 0.1–0.3 mg·mL^{-1}), which are positively charged molecules but without micellar structure, were incubated with ICG under the same condition as for DSPE-PEG_{2k}-NH_2. However, no conversion trend was observed (Figures 1C and S1C). This result indicated that the micellar structure would also be necessary for the ICG J-aggregation. Subsequently, the location of ICG J-aggregates in DSPE-PEG_{2k}-NH_2 micelles was analyzed by ^{1}H NMR. As shown in Figures 1E and S2, for the spectrum I of pure DSPE-PEG_{2k}-NH_2 micelles, the resonances of the hydrophobic DSPE core (b and c) and of the hydrophilic PEG shell (a) were well resolved; also, spectrum III of the naked ICG J-aggregates showed sharp resonances. In spectrum II, for the complex between DSPE-PEG_{2k}-NH_2 micelles and ICG J-aggregates, there were a set of resonance peaks showing the same pattern as that of the naked ICG

J-aggregates but locating at relatively higher field; meanwhile, the resonances of both the DSPE core and the PEG shell of the DSPE-PEG_{2k}-NH_2 micelle became broader and shifted to a higher field region (a′, b′, and c′). All these resonance changes could be attributed to the shielding effect induced by guest encapsulation (Zhao et al., 2008; Hu et al., 2009), which fully demonstrated that the ICG molecules were encapsulated in the DSPE-PEG_{2k}-NH_2 micelles under the aggregated state.

Above all, considering the amphiphilic nature of ICG, it can be arranged in the hydrophilic-hydrophobic interface of the micelle after mixing with the amphiphilic DSPE-PEG (Wan et al., 2014). In other words, the hydrophobic core of micelle will attract the head of ICG inside the micellar structure through hydrophobic interaction. At the same time, the positive charges on the micelle outer surface will attract the negatively charged tail of ICG. As a result, the two forces in opposite directions could preset the orientation of ICG in a head-to-tail fashion and cause the ICG J-aggregation. According to the previous studies, naked ICG J-aggregate requires a long formation time. A high concentration of ICG (~5 $mg \cdot mL^{-1}$) in water could gradually convert to J-aggregate over 1 month (von Berlepsch and Bottcher, 2010), indicating it was a thermodynamically controlled process in the absence of any external forces. We also found that no J-aggregate formed when an aqueous solution of pure ICG at a high concentration (10.0 $mg \cdot mL^{-1}$) was stirred at room temperature for 24 h, whether at pH 4.0 or 7.0 (Figure S3). Here, a kinetically driven J-aggregation of ICG has been revealed by utilizing the host-guest interaction between polymer micelle and ICG molecules, which will significantly facilitate the process. The obtained micellar assembly between ICG J-aggregate and DSPE-PEG_{2k}-NH_2 is denoted as DSPE-PEG@ICG-J. The DSPE-PEG@ICG-J loaded with 33 wt. % ICG J-aggregates was chosen for the following experiments based on careful optimizations (Figure S4). Transmission electron microscopy and dynamic light scattering detections revealed that it was a spherical micelle with an average hydrodynamic diameter of 34.6 nm (Figure 2A), and its zeta potential was −19.3 mV owing to the presence of negatively charged ICG J-aggregates (Liu et al., 2017).

The aggregated ICG in DSPE-PEG@ICG-J showed a sharp absorption at 895 nm, therefore, in contrast to an 808-nm laser generally used for ICG irradiation, an 880-nm laser can be employed to irradiate DSPE-PEG@ICG-J in the related applications. The residual energy of the two beams, from an 808-nm and an 880-nm laser, were compared after they passed through pork slides with different thicknesses (Table S1), where the 880-nm laser exhibited a much better tissue penetration capability. The extinction coefficient by weight of ICG J-aggregates in DSPE-PEG@ICG-J was determined to be 78.0 $L \cdot g^{-1} \cdot cm^{-1}$ at 880 nm, which was much higher than that of free ICG at 808 nm (45.0 $L \cdot g^{-1} \cdot cm^{-1}$) and many other photothermal materials, such as reduced graphene (~22.0 $L \cdot g^{-1} \cdot cm^{-1}$, 808 nm), single-walled carbon nanotubes (~46.5 $L \cdot g^{-1} \cdot cm^{-1}$, 808 nm), and gold nanorods (~13.9 $L \cdot g^{-1} \cdot cm^{-1}$, 808 nm) (Robinson et al., 2010, 2011). Meanwhile, DSPE-PEG@ICG-J showed negligible fluorescence (Figure S5), which probably came from the super-quenching effect of J-aggregates (Lu et al., 2002). Both the enhanced absorption and fluorescence quenching can facilitate the energy conversion from light to heat, therefore at 50 $\mu g \cdot mL^{-1}$ equivalent concentration of ICG, the temperature of DSPE-PEG@ICG-J solution increased from 25.3°C to 71.7°C ($\Delta T \sim 46.4$°C) after a 10-min irradiation at 880 nm, whereas that of free ICG solution increased from 25.2°C to 67.1°C ($\Delta T \sim 41.9$°C) under 808 nm irradiation (Figure 2B). In addition to the superior optical properties, DSPE-PEG@ICG-J also exhibited excellent photostability. After five cycles of irradiation on-off process, DSPE-PEG@ICG-J held a consistent photothermal conversion capability, whereas free ICG (50 $\mu g \cdot mL^{-1}$) could only elevate 18°C in the end (Figure 2C). We noted that, after a 10-min laser irradiation, the absorption of free ICG decayed significantly, indicating the degradation of ICG molecules (Figure 2D); however, under the same irradiation time, the absorption spectrum of DSPE-PEG@ICG-J showed no visible change (Figure 2E).

The naked ICG J-aggregate suffers from poor intracellular and *in vivo* bio-stability (Liu et al., 2017), which was completely overcome by DSPE- PEG@ICG-J. After a 24-h incubation in 10% fetal bovine serum (mimicking the biological condition) or a 12-h incubation with A549 cells, the characteristic absorption of ICG J-aggregate in DSPE-PEG@ICG-J showed no obvious change (Figures 2F and 2G), demonstrating that the molecular structure and the aggregation state of ICG were well reserved. The *in vivo* structural integration of DSPE-PEG@ICG-J was investigated through intravenous injection in mice, and the mice injected with free ICG were tested as control. Emitting NIR fluorescence at 845 nm, free ICG can be detected by *in vivo* fluorescence imaging, which is used to indicate the disassembly of ICG J-aggregates in animal body. For the mice injected with free ICG, obvious fluorescence was detected

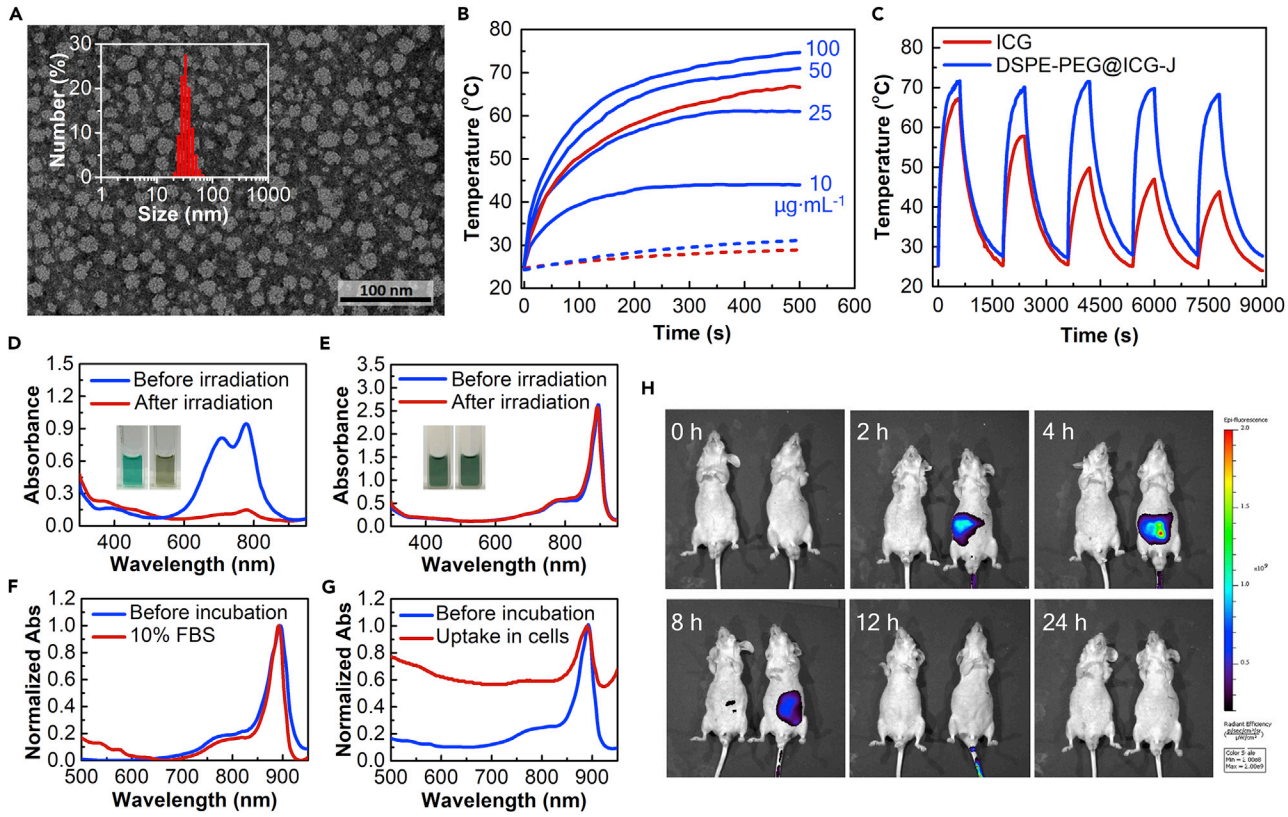

Figure 2. Micelle Morphology, *In Vitro* Photothermal Properties, as well as Photo- and Bio-stability of DSPE-PEG@ICG-J

(A) Transmission electron microscopic image and dynamic light scattering analysis result (inset) of DSPE-PEG@ICG-J.

(B) Temperature profiles of PBS buffer (blue dashed line) and DSPE-PEG@ICG-J solutions at different concentrations (blue solid line) under the irradiation of 880-nm laser (0.8 W·cm^{-2}), as well as of PBS buffer (red dash) and free ICG at 50 μg·mL^{-1} (red solid line) under the irradiation of 808-nm laser (0.8 W·cm^{-2}).

(C–G) (C) The temperature profiles of DSPE-PEG@ICG-J and free ICG at 50 μg·mL^{-1} under five cycles of laser on-off (0.8 W·cm^{-2}; 880-nm laser for DSPE-PEG@ICG-J; 808-nm laser for free ICG). The absorption spectra of (D) free ICG and (E) DSPE-PEG@ICG-J before and after 10-min laser irradiation, and the inserts show the before (left) and after (right) photographs. The stability of DSPE-PEG@ICG-J when incubated in (F) 10% fetal bovine serum or (G) with A549 cells.

(H) The fluorescence profiles of DSPE-PEG@ICG-J (left) and free ICG (right) after they were intravenously injected into mice (150.0 μL, at ICG equivalent concentration of 0.5 mg·mL^{-1}).

See also Figures S4 and S5.

post injection and before the complete metabolism. On the other hand, for the mice injected with DSPE-PEG@ICG-J, no detectable fluorescence was observed during a 24-h period (Figure 2H). Thus the ICG J-aggregates in DSPE-PEG@ICG-J complex micelles show robust stabilities under intracellular and *in vivo* incubations.

Compared with the naked ICG J-aggregate, DSPE-PEG@ICG-J is convenient to be modified for multi-functionalization, which is another benefit of the hierarchical assembly. First, the amine groups on the PEG shell, which were necessary for the formation of ICG J-aggregate, were utilized to conjugate cancer-targeting ligand after the formation of the complex micelle. A DNA aptamer, AS1411, was selected, which could recognize nucleolin, a specific cellular protein commonly overexpressed on cancer cell membranes (Li et al., 2017). Through NHS/EDC amidation reaction, a high density of AS1411 aptamers (~114 μmol·g^{-1}) could be coupled on the surface of DSPE-PEG@ICG-J (the product was named as DSPE-PEG-1411@ICG-J). Second, due to the negatively charged surface of the complex micelle, a large quantity of positively charged DOX for chemotherapy could be loaded through electrostatic interactions (~0.2 g DOX on 1.0 g of DSPE-PEG@ICG-J) (Scheme 1). We found that the AS1411 conjugation and DOX loading did not alter the aggregation state of ICG (Figure S6A). The fully functionalized micelle was named as DSPE-PEG-1411@ICG-J/DOX, which showed a hydrodynamic diameter enlarged to 48.4 nm (inset of

Figure S6B) and an electrically neutral surface (−1.3 mV). The photothermal properties as well as the photo- and bio-stabilities of this multifunctional micelle were fully characterized according to the same procedures for DSPE-PEG@ICG-J, and its performances were consistent with those of DSPE-PEG@ICG-J in all the tests (Figures S7A–S7D), which demonstrated that the incorporation with DOX and DNA aptamer did not affect the photothermal and structural properties of the complex micelle. Subsequently, DOX release from DSPE-PEG-1411@ICG-J/DOX was monitored over a period of 72 h in PBS buffer (pH 7.4) and HAc-NaAc buffer (pH 5.5), which mimicked the pH values of blood and tumor endosome, respectively (Zheng et al., 2016). The DOX release at pH 5.5 was much quicker than that at pH 7.4; in the end, ~ 90% DOX was released at pH 5.5, whereas only ~49% of DOX could be released at pH 7.4 (Figure S7E). These results demonstrated that the DOX release from DSPE-PEG-1411@ICG-J/DOX exhibited a sustained and pH-responsive nature. Taking into account that the *in vivo* application of the micelles would span several weeks, we further evaluated the long-term stability of the micelles at 37°C for 5 weeks. The PBS dispersions of DSPE-PEG@ICG-J, DSPE-PEG-1411@ICG-J, and DSPE-PEG-1411@ICG-J/DOX all maintained excellent colloidal stability at the endpoint, and there is no significant change in their characteristic absorption and the average hydrodynamic diameter of the micelles (Figure S8).

Anticancer Therapy

After coupling with AS1411 aptamer, the cell uptake amount of the complex micelles was about 2.6 times higher than that of their unfunctionalized counterpart on human lung carcinoma A549 cell line overexpressing nucleolin on the cell membrane (Figure S9) (Li et al., 2014). Coupling with the active targeting, ICG J-aggregate-dominated PTT, and DOX-dominated chemotherapy, DSPE-PEG-1411@ICG-J/DOX could kill 99.2% A549 cells at an ICG equivalent concentration of 100 $\mu g \cdot mL^{-1}$ under a 10-min 880-nm laser irradiation (0.8 $W \cdot cm^{-2}$) (Figures S10 and S11). Therefore, the *in vivo* anti-tumor efficacies of the micelles based on ICG J-aggregate were systematically evaluated on A549 tumor-bearing BALB/c nude mice. The tumor accumulations of the micelles following intravenous injection were visualized by PAI. Before the *in vivo* PAI, the concentration-dependent photoacoustic signal of the micelles had been confirmed by the *in vitro* studies (Figure S12). All the micelles, DSPE-PEG@ICG-J, DSPE-PEG-1411@ICG-J, and DSPE-PEG-1411@ICG-J/DOX, showed time-dependent accumulation at tumor tissues and reached peak levels at 12 h post the injection (Figure 3A). Therefore, 12 h post administration was an ideal time point for micelles, whereas the PTT time point for ICG was determined to be 1 h after intravenous administration according to the *in vivo* fluorescence imaging (Figure S13). Subsequently, we examined the tumoral temperature profiles during the *in vivo* PTT. As shown in Figure 3B, infrared thermography disclosed that the surface temperatures of the tumors in mice treated with DSPE-PEG@ICG-J, DSPE-PEG-1411@ICG-J, and DSPE-PEG-1411@ICG-J/DOX rapidly increased to over 50°C in 4 min and reached peak temperatures of 51.2°C, 54.2°C, and 53.8°C, respectively. In contrast, the highest temperature of the tumor in free ICG-treated mouse reached 44.7°C. The tumor site of PBS-treated mouse showed slight temperature elevation under irradiation, proving no background interference here. It has been reported that strong photothermal heating, which raises the tumor local temperature over 48°C, will result in irreversible tissue damage, whereas the tumor temperature between 40°C and 45°C can only bring sublethal damage to tumor cells (Yoo et al., 2013). This declaration was proved by the histopathological tissue analysis following H&E staining of tumor sections from mice after the PTT treatments. As shown in Figure 4A, compared with free ICG, DSPE-PEG@ICG-J and DSPE-PEG-1411@ICG-J resulted in more necrotic areas at the tumor. Moreover, compared with its counterpart without AS1411 conjugation, DSPE-PEG-1411@ICG-J led to severe tumor damage. Therefore, compared with free ICG, the strengthened light absorption and superior stability of the ICG J-aggregate, as well as the increased tumor accumulation through the EPR effect (Blanco et al., 2015; Stylianopoulos, 2013) and AS1411 active targeting, could indeed improve the PTT performance of the micelles.

Finally, A549 tumor-bearing mice were randomly divided into nine groups to comprehensively evaluate the *in vivo* therapeutic efficacies of the micelles over a 24-day follow-up period. Groups with and without laser irradiation are marked with [+] and [-], respectively; therefore the 9 groups include: (i) control (without any treatment); (ii) [-] DOX; (iii) [+] PBS, 880-nm laser; (iv) [+] ICG, 808-nm laser; (v) [-] Doxil (a clinically approved liposomal doxorubicin formulation); (vi) [-] DSPE-PEG-1411@ICG-J/DOX; (vii) [+] DSPE-PEG@ICG-J, 880-nm laser; (viii) [+] DSPE-PEG-1411@ICG-J, 880-nm laser; (ix) [+] DSPE-PEG-1411@ICG-J/DOX, 880-nm laser. As shown in Figure 4B and 4C and Figures S14A and B, for mice in the two control groups (i) and (iii), the tumors eventually increased 7- to 9-fold in volume. Free ICG in group (iv) exhibited poor photothermal therapeutic efficiency, which was probably due to the instability and quick metabolism of ICG

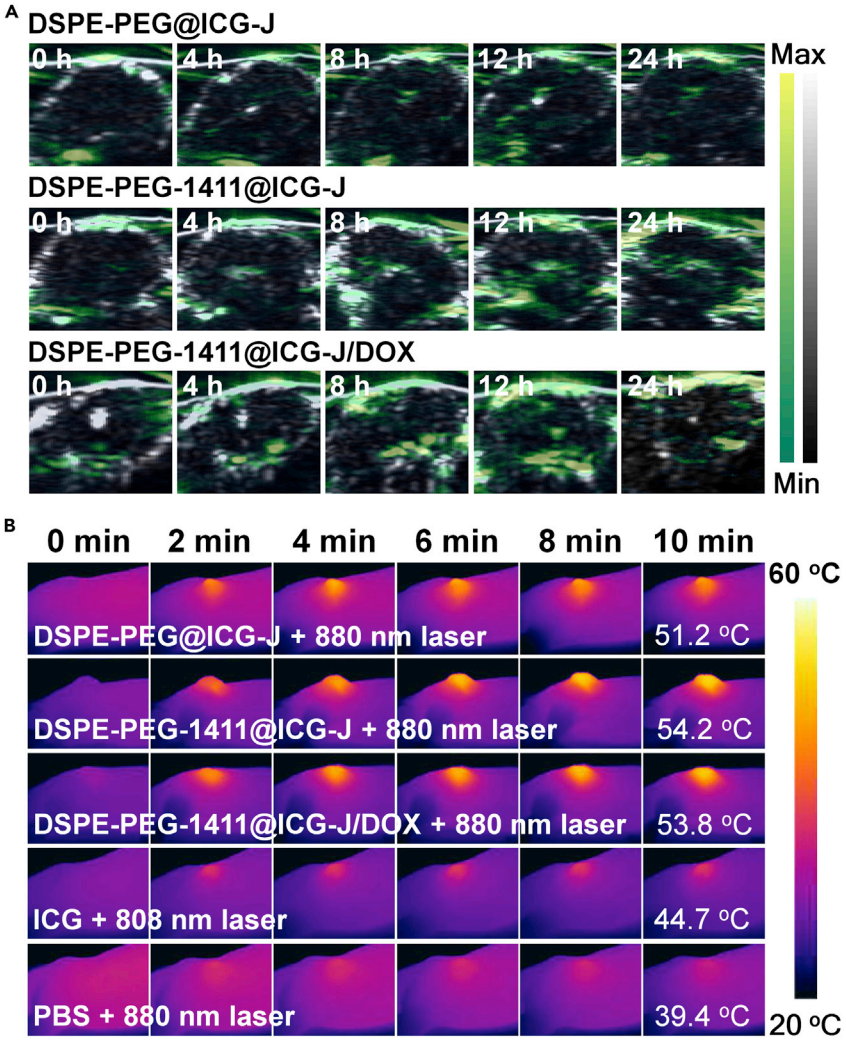

Figure 3. Detecting Tumor Accumulation of the Micelles through PAI and Monitoring Temperature Changes of the Tumors in the *In Vivo* PTT Process

(A) Time-dependent tumor site photoacoustic images (yellow-green scale) of the A549 tumor-bearing mice intravenously injected with various samples; the tumor boundaries were delineated by ultrasound images (gray scale). A pulsed 880-nm laser was used as excitation source, and the induced photoacoustic waves were collected by a point-focused 7.5-MHz ultrasound transducer.

(B) The infrared (IR) thermography of the tumors from A549 tumor-bearing mice intravenously injected with various samples at different time points after laser irradiation (the power density of both 808- and 880-nm lasers is 0.8 W cm^{-2}). In both the photoacoustic imaging and the IR thermography experiments, the intravenous injection volume of the samples is 150.0 μL; for ICG and the micelles, ICG concentration equivalent to 0.5 mg·mL^{-1}.

See also Table S1, Figures S6–S8, S12, S13, and S18.

molecules. After the assembly, significantly improved PTT efficiency was observed in group (vii), where the tumor growth rate was greatly inhibited (only ~2.3-fold increase). Notably, through the introduction of AS1411 aptamer, DSPE-PEG-1411@ICG-J in group (viii) realized complete tumor ablation at the beginning, although tumor reoccurred at the end, which demonstrated the important role of AS1411 aptamer in active targeting to enhance accumulation of micellar medicines inside tumor. As a direct evidence, the bio-distribution determination 12 h after intravenous injection of the micelles indicated that the intra-tumor accumulation efficiency of DSPE-PEG@ICG-J was 3.00% ID·g^{-1}, whereas benefiting from the active targeting ability of AS1411 aptamer, the accumulation amounts of DSPE-PEG-1411@ICG-J and DSPE-PEG-1411@ICG-J/DOX increased to 4.23% and 4.11% ID·g^{-1}, respectively (Figure S14C). Compared with free DOX in group (ii) and Doxil in group (v), the chemotherapeutic efficiency was greatly improved when

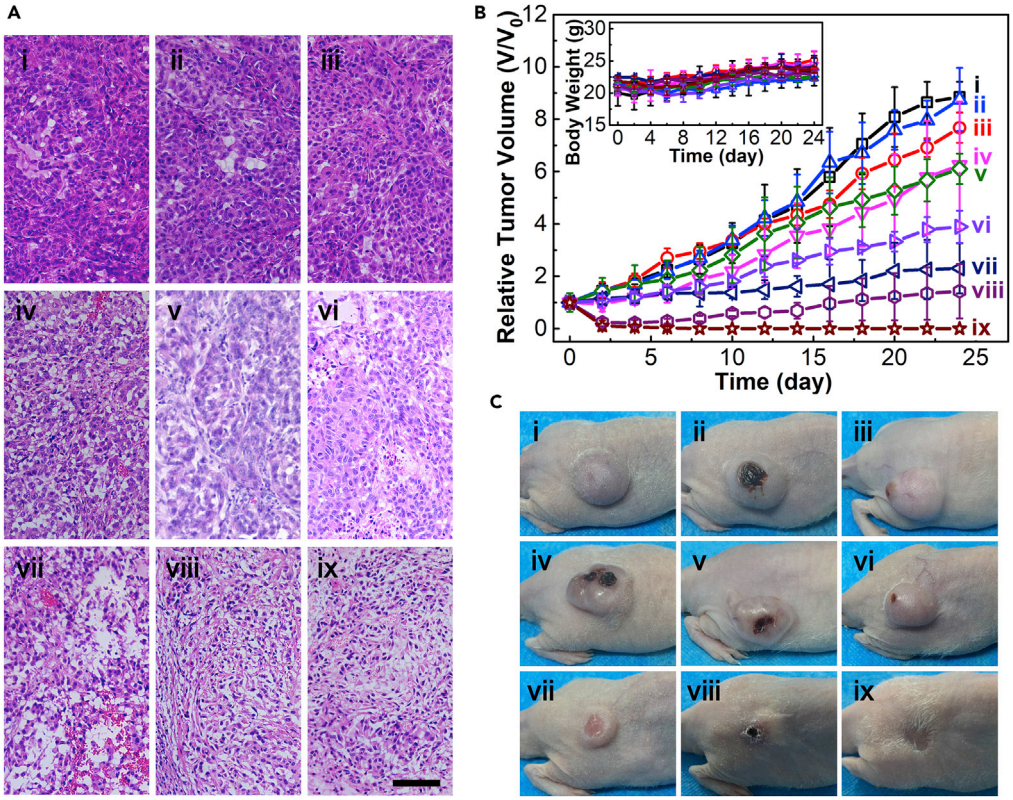

Figure 4. *In Vivo* Anticancer Therapy Record

(A) H&E-stained slices of tumors collected from A549 tumor-bearing mice 12 h after receiving the treatments. Scale bar, 100 μm.

(B) Tumor growth curves and the body weight (inset) of the mice in different groups; data are presented as the average ± SD (n = 3).

(C) Photographs of mice in different groups at the end of treatments. The samples in (A–C): (i) control (without any treatment); (ii) [-] DOX; (iii) [+] PBS; (iv) [+] ICG; (v) [-] Doxil; (vi) [-] DSPE-PEG-1411@ICG-J/DOX; (vii) [+] DSPE-PEG@ICG-J; (viii) [+] DSPE-PEG-1411@ICG-J; and (ix) [+] DSPE-PEG-1411@ICG-J/DOX; [+] and [-] stand for laser-irradiated and non-laser-irradiated groups, respectively; 808-nm laser was used for group (iv) and 880-nm laser was used for the other groups. The power density of both 808- and 880-nm lasers is 0.8 W cm^{-2}. In the experiment, intravenous injection volume of the samples is 150.0 μL; for ICG and the micelles, ICG concentration equivalent to 0.5 mg·mL^{-1}; for DOX and Doxil, DOX concentration equivalent to 0.3 mg·mL^{-1}.

See also Table S1, Figures S6–S11 and S14–S18.

DOX was loaded on the micelle coupled with AS1411 active targeting in group (vi), which was consistent with the histopathological tissue analysis. Free DOX and Doxil, respectively, caused negligible and slight injury to the tumor, whereas for DSPE-PEG-1411@ICG-J/DOX in group (vi), even without laser irradiation, more visible injury to the tumor was observed (Figure 4A). To the end, [+] DSPE-PEG-1411@ICG-J/DOX in group (ix), which synergistically combined active targeting, PTT, and chemotherapy, displayed the best therapeutic effect, with complete tumor elimination and no local reoccurrence during the 24-day period. The mice in all the treatment groups did not show weight loss (inset of Figure 4B) or other abnormality during the whole process, suggesting that both ICG and micelles showed negligible acute toxicity for *in vivo* applications. Subsequently, a blood circulation analysis of DSPE-PEG-1411@ICG-J/DOX was conducted on Sprague Dawley rats; the result showed that the half-life time of the micelle in blood was ~6.5 h (Figure S15), whereas that of ICG is just 2–4 min (Mundra et al., 2015). This long blood circulation property can strengthen the tumor accumulation of the micelle through EPR effect (Robinson et al., 2012). Furthermore, we found that one week after the intravenous injection of DSPE-PEG-1411@ICG-J/DOX, there was almost no ICG in the main organs of mice (Figure S16), which means the micelles had been completely metabolized and would have no potential toxicity to the mice. The histopathological analysis and the blood routine test on the healed mice in group (ix) confirmed this inference. We found that, after the treatment,

the mice showed no visible signs of damage in the main organs (Figure S17A) and had normal blood parameters with no statistical difference to those of the healthy mice (Figure S17B). These results convinced that, in addition to the superior therapeutic performance, DSPE-PEG-1411@ICG-J/DOX is also a safe and reliable organic medicine without long-term toxicity and side effects.

Conclusion

We revealed that through a hierarchical assembly with micelle polymer, ICG can efficiently convert to J-aggregate in several hours without a high-concentration requirement. The careful investigation demonstrated that the amphiphilic structure of the micelle and the positive charge on the micelle surface were crucial in this process, which synergistically afforded electrostatic and hydrophobic attractions to the negatively charged amphiphilic ICG molecules, so that the molecules could be concentrated and arranged in the head-to-tail fashion in the micelle. Compared with free ICG, the as-fabricated DSPE-PEG@ICG-J complex micelle exhibited some advanced properties for cancer theranostics, including (1) an 880-nm laser with higher tissue penetration depth could be used for phototheranostics, (2) enhanced photothermal conversion resulted in a higher PTT efficiency, (3) robust photo- and bio-stability, and (4) excellent functional scalability through covalent grafting as well as physisorption. Based on DSPE-PEG@ICG-J, a multifunctional micellar medicine, DSPE-PEG-1411@ICG-J/DOX, was finally fabricated, which combined with J-aggregation-enhanced PTT, aptamer and EPR-effect-promoted tumor enrichment, and chemotherapy based on DOX sustained release, could promote complete tumor elimination with no local reoccurrence and without long-term toxicity or side effects during a 24-day period. To the best of our knowledge, this is the first report of controlling the J-aggregation of a classical clinical dye in polymer micelles to achieve enhanced properties. Like "old wine in a new bottle," many "old" materials, which have been developed and well studied at the molecular level, will probably show new opportunity at the supramolecular level.

Limitations of the Study

In this study, we first report the method of controlling the J-aggregation of a cyanine dye within amphiphilic polymer micelles; however, only ICG as the cyanine dye model has been investigated. In future work, the applicability of this method to other NIR dyes and amphiphilic polymer will be investigated.

METHODS

All methods can be found in the accompanying Transparent Methods supplemental file.

SUPPLEMENTAL INFORMATION

Supplemental Information can be found online at https://doi.org/10.1016/j.isci.2019.11.022.

ACKNOWLEDGMENTS

The authors acknowledge financial support by grants from Shenzhen Fundamental Research Programs (No. JCYJ20160226193029593, No. JCYJ20170817105645935), Shenzhen Science and Technology Innovation Commission (Grant No. KQTD20170810111314625), Guangdong Innovative and Entrepreneurial Research Team Program (No. 2016ZT06G587), and the National Natural Science Foundation of China (No. 51503096).

AUTHOR CONTRIBUTIONS

L.T. and C.S. conceived the project and designed the experiments. C.S. and D.J. carried out the experiments of material fabrication and characterizations; C. S., J.Y., and F.X. carried out the cellular and *in vivo* experiments; H.G. and L.X. carried out photoacoustic imaging experiments; L.T. and C.S. analyzed the data and co-wrote the manuscript with input from the other co-authors. All authors discussed the results and commented on the manuscript.

DECLARATION OF INTERESTS

The authors declare no competing financial interests.

Received: May 8, 2019
Revised: November 10, 2019
Accepted: November 12, 2019
Published: December 20, 2019

REFERENCES

Blanco, E., Shen, H., and Ferrari, M. (2015). Principles of nanoparticle design for overcoming biological barriers to drug delivery. Nat. Biotechnol. *33*, 941–951.

Cai, X.L., Mao, D., Wang, C., Kong, D.L., Cheng, X.M., and Liu, B. (2018a). Multifunctional liposome: a bright AIEgen-lipid conjugate with strong photosensitization. Angew. Chem. Int. Ed. *57*, 16396–16400.

Cai, Y., Si, W.L., Huang, W., Chen, P., Shao, J.J., and Dong, X.C. (2018b). Organic dye based nanoparticles for cancer phototheranostics. Small *14*, 1704247.

Cai, K., Xie, J.J., Zhang, D., Shi, W.J., Yan, Q.F., and Zhao, D.H. (2018c). Concurrent cooperative J-aggregates and anticooperative H-aggregates. J. Am. Chem. Soc. *140*, 5764–5773.

Chen, Z.J., Liu, Y., Wagner, W., Stepanenko, V., Ren, X.K., Ogi, S., and Wurthner, F. (2017). Near-IR absorbing J-aggregate of an amphiphilic BF2-azadipyrromethene dye by kinetic cooperative self-assembly. Angew. Chem. Int. Ed. *56*, 5729–5733.

Coles, D.M., Meijer, A.J.H.M., Tsoi, W.C., Charlton, M.D.B., Kim, J.-S., and Lidzey, D.G. (2010). A characterization of the Raman modes in a J-aggregate-forming dye: a comparison between theory and experiment. J. Phys. Chem. A *114*, 11920–11927.

Egawa, Y., Hayashida, R., and Anzai, J.I. (2007). pH-induced interconversion between J-aggregates and H-aggregates of 5,10,15,20-tetrakis(4-sulfonatophenyl)porphyrin in polyelectrolyte multilayer films. Langmuir *23*, 13146–13150.

Eisele, D.M., Cone, C.W., Bloemsma, E.A., Vlaming, S.M., van der Kwaak, C.G.F., Silbey, R.J., Bawendi, M.G., Knoester, J., Rabe, J.P., and Vanden Bout, D.A. (2012). Utilizing redox-chemistry to elucidate the nature of exciton transitions in supramolecular dye nanotubes. Nat. Chem. *4*, 655–662.

Gaufres, E., Tang, N.Y.W., Lapointe, F., Cabana, J., Nadon, M.A., Cottenye, N., Raymond, F., Szkopek, T., and Martel, R. (2014). Giant Raman scattering from J-aggregated dyes inside carbon nanotubes for multispectral imaging. Nat. Photonics *8*, 73–79.

Gorl, D., Zhang, X., and Wurthner, F. (2012). Molecular assemblies of perylene bisimide dyes in water. Angew. Chem. Int. Ed. *51*, 6328–6348.

Guo, Z.Q., Park, S., Yoon, J., and Shin, I. (2014). Recent progress in the development of near-infrared fluorescent probes for bioimaging applications. Chem. Soc. Rev. *43*, 16–29.

He, H., Ji, S.S., He, Y., Zhu, A.J., Zou, Y.L., Deng, Y.B., Ke, H.T., Yang, H., Zhao, Y.L., Guo, Z.Q., et al. (2017). Photoconversion-tunable fluorophore vesicles for wavelength-dependent photoinduced cancer therapy. Adv. Mater. *29*, 1606690.

Horn, D., and Rieger, J. (2001). Organic nanoparticles in the aqueous phase - theory, experiment, and use. Angew. Chem. Int. Ed. *40*, 4331–4361.

Hu, J.J., Cheng, Y.Y., Ma, Y.R., Wu, Q.L., and Xu, T.W. (2009). Host-guest chemistry and physicochemical properties of the dendrimer-mycophenolic acid complex. J. Phys. Chem. B *113*, 64–74.

Huang, P., Gao, Y., Lin, J., Hu, H., Liao, H.S., Yan, X.F., Tang, Y.X., Jin, A., Song, J.B., Niu, G., et al. (2015). Tumor-specific formation of enzyme-instructed supramolecular self-assemblies as cancer theranostics. ACS Nano *9*, 9517–9527.

Jiao, Y., Liu, K., Wang, G.T., Wang, Y.P., and Zhang, X. (2015). Supramolecular free radicals: near-infrared organic materials with enhanced photothermal conversion. Chem. Sci. *6*, 3975–3980.

Kim, T.I., Hwang, B., Lee, B., Bae, J., and Kim, Y. (2018). Selective monitoring and imaging of eosinophil peroxidase activity with a J-aggregating probe. J. Am. Chem. Soc. *140*, 11771–11776.

Li, L.Y., Hou, J.J., Liu, X.J., Guo, Y.J., Wu, Y., Zhang, L.H., and Yang, Z.J. (2014). Nucleolin-targeting liposomes guided by aptamer AS1411 for the delivery of siRNA for the treatment of malignant melanomas. Biomaterials *35*, 3840–3850.

Li, F.F., Lu, J., Liu, J., Liang, C., Wang, M.L., Wang, L.Y., Li, D.F., Yao, H.Z., Zhang, Q.L., Wen, J., et al. (2017). A water-soluble nucleolin aptamer-paclitaxel conjugate for tumor-specific targeting in ovarian cancer. Nat. Commun. *8*, 1390.

Liu, R., Tang, J., Xu, Y., Zhou, Y., and Dai, Z. (2017). Nano-sized indocyanine green J-aggregate as a one-component theranostic agent. Nanotheranostics *1*, 430–439.

Lovell, J.F., Jin, C.S., Huynh, E., Jin, H.L., Kim, C., Rubinstein, J.L., Chan, W.C.W., Cao, W.G., Wang, L.V., and Zheng, G. (2011). Porphysome nanovesicles generated by porphyrin bilayers for use as multimodal biophotonic contrast agents. Nat. Mater. *10*, 324–332.

Lu, L.D., Jones, R.M., McBranch, D., and Whitten, D. (2002). Surface-enhanced superquenching of cyanine dyes as J-aggregates on laponite clay nanoparticles. Langmuir *18*, 7706–7713.

Luo, S.L., Zhang, E.L., Su, Y.P., Cheng, T.M., and Shi, C.M. (2011). A review of NIR dyes in cancer targeting and imaging. Biomaterials *32*, 7127–7138.

Mundra, V., Peng, Y., Rana, S., Natarajan, A., and Mahato, R.I. (2015). Micellar formulation of indocyanine green for phototherapy of melanoma. J. Control Release *220*, 130–140.

Porcu, E.P., Salis, A., Gavini, E., Rassu, G., Maestri, M., and Giunchedi, P. (2016). Indocyanine green delivery systems for tumour detection and treatments. Biotechnol. Adv. *34*, 768–789.

Pu, K.Y., Shuhendler, A.J., Jokerst, J.V., Mei, J.G., Gambhir, S.S., Bao, Z.N., and Rao, J.H. (2014). Semiconducting polymer nanoparticles as photoacoustic molecular imaging probes in living mice. Nat. Nanotechnol. *9*, 233–239.

Qi, J., Fang, Y., Kwok, R.T.K., Zhang, X.Y., Hu, X.L., Lam, J.W.Y., Ding, D., and Tang, B.Z. (2017). Highly stable organic small molecular nanoparticles as an advanced and biocompatible phototheranostic agent of tumor in living mice. ACS Nano *11*, 7177–7188.

Robinson, J.T., Welsher, K., Tabakman, S.M., Sherlock, S.P., Wang, H.L., Luong, R., and Dai, H.J. (2010). High performance *in vivo* near-IR (> 1 μm) imaging and photothermal cancer therapy with carbon nanotubes. Nano Res. *3*, 779–793.

Robinson, J.T., Tabakman, S.M., Liang, Y.Y., Wang, H.L., Casalongue, H.S., Vinh, D., and Dai, H.J. (2011). Ultrasmall reduced graphene oxide with high near-infrared absorbance for photothermal therapy. J. Am. Chem. Soc. *133*, 6825–6831.

Robinson, J.T., Hone, G., Liang, Y., Zhang, B., Yaghi, O.K., and Dai, H. (2012). In vivo fluorescence imaging in the second near-infrared window with long circulating carbon nanotubes capable of ultrahigh tumor uptake. J. Am. Chem. Soc. *134*, 10664–10669.

Sengupta, S., and Würthner, F. (2013). Chlorophyll J-aggregates: from bioinspired dye stacks to nanotubes, liquid crystals, and biosupramolecular electronics. Acc. Chem. Res. *46*, 2498–2512.

Sheng, Z.H., Hu, D.H., Xue, M.M., He, M., Gong, P., and Cai, L.T. (2013). Indocyanine green nanoparticles for theranostic applications. Nano Micro Lett. *5*, 145–150.

Song, X.J., Gong, H., Liu, T., Cheng, L., Wang, C., Sun, X.Q., Liang, C., and Liu, Z. (2014). J-aggregates of organic dye molecules complexed with iron oxide nanoparticles for imaging-guided photothermal therapy under 915-nm light. Small *10*, 4362–4370.

Song, X.J., Chen, Q., and Liu, Z. (2015a). Recent advances in the development of organic photothermal nano-agents. Nano Res. *8*, 340–354.

Song, X.J., Zhang, R., Liang, C., Chen, Q., Gong, H., and Liu, Z. (2015b). Nano-assemblies of J-aggregates based on a NIR dye as a multifunctional drug carrier for combination cancer therapy. Biomaterials *57*, 84–92.

Song, Q., Jiao, Y., Wang, Z.Q., and Zhang, X. (2016). Tuning the energy gap by supramolecular approaches: towards near-infrared organic assemblies and materials. Small *12*, 24–31.

Stylianopoulos, T. (2013). EPR-effect: utilizing size-dependent nanoparticle delivery to solid tumors. Ther. Deliv. *4*, 421–423.

Su, M.H., Li, S.X., Zhang, H., Zhang, J.Q., Chen, H.L., and Li, C.H. (2019). Nano-assemblies from J-aggregated dyes: a stimuli-responsive tool applicable to living systems. J. Am. Chem. Soc. *141*, 402–413.

Varughese, S. (2014). Non-covalent routes to tune the optical properties of molecular materials. J. Mater. Chem. C *2*, 3499–3516.

von Berlepsch, H., and Bottcher, C. (2010). Cryo-transmission electron microscopy reveals mesoscopic H- and J-aggregates of near infrared

cyanine dyes. J. Photochem. Photobiol. A *214*, 16–21.

von Berlepsch, H., Kirstein, S., Hania, R., Pugzlys, A., and Bottcher, C. (2007). Modification of the nanoscale structure of the J-aggregate of a sulfonate-substituted amphiphilic carbocyanine dye through incorporation of surface-active additives. J. Phys. Chem. B *111*, 1701–1711.

Walker, B.J., Dorn, A., Bulovic, V., and Bawendi, M.G. (2011). Color-selective photocurrent enhancement in coupled J-aggregate/nanowires formed in solution. Nano Lett. *11*, 2655–2659.

Wan, Z.H., Mao, H.J., Guo, M., Li, Y.L., Zhu, A.J., Yang, H., He, H., Shen, J.K., Zhou, L.J., Jiang, Z., et al. (2014). Highly efficient hierarchical micelles integrating photothermal therapy and singlet oxygen-synergized chemotherapy for cancer eradication. Theranostics *4*, 399–411.

Wurthner, F., Kaiser, T.E., and Saha-Moller, C.R. (2011). J-aggregates: from serendipitous discovery to supramolecular engineering of functional dye materials. Angew. Chem. Int. Ed. *50*, 3376–3410.

Yin, L., Sun, H., Zhang, H., He, L., Qiu, L., Lin, J.G., Xia, H.W., Zhang, Y.Q., Ji, S.J., Shi, H.B., et al. (2019). Quantitatively visualizing tumor-related protease activity *in vivo* using a ratiometric photoacoustic probe. J. Am. Chem. Soc. *141*, 3265–3273.

Yoo, D., Jeong, H., Noh, S.-H., Lee, J.-H., and Cheon, J. (2013). Magnetically triggered dual functional nanoparticles for resistance-free apoptotic hyperthermia. Angew. Chem. Int. Ed. *52*, 13047–13051.

Zhao, L.Z., Ma, R.J., Li, J.B., Li, Y., An, Y.L., and Shi, L.Q. (2008). J- and H-aggregates of 5,10,15,20-tetrakis-(4-sulfonatophenyl)-porphyrin and interconversion in PEG-b-P4VP micelles. Biomacromolecules *9*, 2601–2608.

Zheng, M., Yue, C., Ma, Y., Gong, P., Zhao, P., Zheng, C., Sheng, Z., Zhang, P., Wang, Z., and Cai, L. (2013). Single-step assembly of DOX/ICG loaded lipid-polymer nanoparticles for highly effective chemo-photothermal combination therapy. ACS Nano *7*, 2056–2067.

Zheng, T.T., Li, G.G., Zhou, F., Wu, R., Zhu, J.J., and Wang, H. (2016). Gold-nanosponge-based multistimuli-responsive drug vehicles for targeted chemo-photothermal therapy. Adv. Mater. *28*, 8218–8226.

ISCI, Volume *22*

Supplemental Information

Utilizing Polymer Micelle to Control Dye J-aggregation and Enhance Its Theranostic Capability

Chen Shao, Fan Xiao, Heng Guo, Jiantao Yu, Dong Jin, Changfeng Wu, Lei Xi, and Leilei Tian

TRANSPARENT METHODS

Chemicals and materials. Chemicals and solvents were used as received without further purification, unless specified otherwise. DNA sequences (HPLC purified), thiazolyl blue tetrazolium bromide (MTT), calcein acetoxymethyl ester (Calcein-AM), propidium iodide (PI), and tubular dialyzer (50,000-molecular-weight cutoff, 2.5 mL) were obtained from Sangon Biotech Co., Ltd. (Shanghai, China). Indocyanine green (ICG) was purchased from TCI Chemical Industry Co., Ltd. (Japan). DSPE-PEG_{2k}-NH_2 was purchased from Shanghai Ponsure Biotech, Inc. (Shanghai, China). Acetic acid (HAc), sodium acetate (NaAc), doxorubicin hydrochloride (DOX), 4-Morpholineethanesulfonic acid (MES), 1-(3-(dimethylamino) propyl)-3-ethylcarbodiimide hydrochloride (EDC), N-hydroxysulfosuccinimide (NHS), and dimethyl sulfoxide (DMSO) were obtained from Aladdin Chemistry Co., Ltd. (Shanghai, China). The acetic acid and N, N-diethylethanamine for preparing triethylammonium acetate buffer (TEAA), and the acetonitrile used in HPLC analysis were of HPLC grade and purchased from Energy Chemical Co., Ltd. (Shanghai, China). Doxil was obtained from the Shenzhen Second People's Hospital. Phosphate buffered saline (PBS) was prepared by dissolving tablets obtained from Amresco (Solon, OH, USA) in ultrapure water according to the manufacturer's instructions (10.0 mM PBS, containing 137.0 mM Na^+ and 2.0 mM K^+). Acetyl acetate solution (3.0%) and copper grid were purchased from Zhongjingkeyi Technology Co., Ltd. (Beijing, China). Ultrapure water (at 18.2 MOhm) was produced by a Millipore synergy UV Ultrapure water purification system (MA, USA). The ultrafiltration tube (100,000-molecular-weight cutoff, 15.0 mL) was also purchased from the Millipore Co. Ltd. A549 cells were kindly provided by Professor Ying Sun at the Department of Biology of Southern University of Science and Technology (SUSTech); L02 cells were purchased from Jennio Biotech Co., Ltd. (Guangzhou, China). RPMI 1640 medium, Dulbecco's modified

Eagle's medium (DMEM), trypsin-EDTA solution, fetal bovine serum (FBS), and penicillin/streptomycin were purchased from Gibco BRL Co., Ltd. (Grand Island, NY, USA). Male BALB/c nude mice and SD rats were purchased from Vital River Laboratory Animal Technology Co., Ltd. (Beijing, China).

Instruments. The 808- and 880-nm continuous-wave laser systems were purchased from Changchun Laser Technology Co., Ltd. (Changchun, China). The output power of the lasers was measured with a VLP-2000 laser power meter (Xi'an Hirsh Laser Tech. Co., Ltd., China). The transmission electron microscopy (TEM) images were carried out on Hitachi HT7700 (Hitachi, Japan); the samples were negatively stained with acetyl acetate and imaged by TEM. Specifically, a sample (5.0 μL) was dropped on the surface of a freshly plasma treated copper grid and kept for 2 min, and then the grid was blotted from the edge with a piece of filter paper; thereafter, 5.0 μL of acetyl acetate (1%) was dropped on the sample and kept for 2 min, and again the grid was blotted from the edge with a piece of filter paper to remove the excess acetyl acetate. The grids were completely dried in a vacuum oven prior to the test. The hydrodynamic diameters and zeta potentials of the micelles were determined by a NanoBrook ZetaPALS potential analyzer (Brookhaven Instruments Corporation, USA) in ultrapure water. The absorption calibration curve of ICG and the related absorption analysis, as well as the fluorescence calibration curves of DOX and Cy3-AS1411-COOH and the related fluorescence analysis were carried out on a Cytation 3 microplate reader (BioTek Instruments, Inc., Winooski, USA). The fluorescence spectra were taken by an iHR320 imaging spectrometer (Horiba, Japan). The ^{1}H NMR spectra were recorded on a Bruker Advance 400 instrument in D_2O using the residual signal from H_2O (^{1}H, $\delta = 4.79$ ppm) as the internal standard. The fluorescence images of cells were taken by a Leica TCS-SP8 laser scanning confocal microscope (LSCM, Leica, Germany) with excitation wavelengthes of 488 nm

(for Calcein-AM) and 561 nm (for PI). The *in vivo* fluorescence images were obtained by an IVIS Spectrum Imaging System (PerkinElmer, USA), with an excitation wavelength at 745 nm and the emission wavelength at 850 nm. In the photoacoustic imaging (PAI) experiments, a pulsed OPO laser (Surelite OPO, Continuum, CA, USA) pumped by a Q-switched Nd: YAG laser (Surelite I-20, Continuum, CA, USA) with a duration of 20 ns and a repetition rate of 20 Hz served as the photoacoustic excitation source. The laser beam was split and coupled into two optical fiber bundles. Induced photoacoustic waves were collected by a point-focused 7.5-MHz ultrasound transducer with 0.5-inch aperture and 1.0-inch focal length. The imaging interface consisting of transducer and optical fiber bundles was mounted on a two-dimensional (2D) moving stage that scanned two-dimensionally. The interval step was 0.1 mm in the scanning processes. The quantification analysis was performed by drawing the region of interests (ROIs) over the sample on the PAI images, and then measured the PAI signal intensity using Matlab (MathWorks Inc., MA, USA). The IR thermographic images were taken by a near infrared thermal imager (FLIR-E64501, FLIR Systems Inc., USA). An ACQUITY HPLC system (Waters Corporation, MA, USA) was employed for ICG-quantitation in the bio-distribution measurement. The blood routine test was conducted on a HF-3800 automated hematology analyzer (Healife, China) according to the operating instruction. The H&E stained tissue slices were examined by an Eclipse Ti-S optical microscope (Nikon, Japan).

Fabrication of DSPE-PEG@ICG-J. In a typical process, ICG (50 $\mu g \cdot mL^{-1}$) and DSPE-PEG_{2k}-HN_2 (0.1 $mg \cdot mL^{-1}$) were co-dissolved in ultrapure water; the mixture was heated at 80 ℃ for 15 min with vigorous stirring, and then stirred at room temperature for 8 h. The product was concentrated by ultrafiltration and stored at -4 ℃ for further use.

Fabrication of DSPE-PEG-1411@ICG-J/DOX. In a typical process, 1.0 mL of DSPE-PEG@ICG-J solution (1.5 $mg \cdot mL^{-1}$), 0.3 mL of EDC solution (1.5 M), 0.3 mL of NHS solution (1.5 M), and 50 μL of AS1411-COOH solution (200 μM) were mixed in 2.5 mL of MES buffer (0.5 M, pH 6.75) that containing 2.0 M of NaCl. The mixture was stirred at room temperature for 3 h, and ultra-filtrated to remove the small molecules and unreacted AS1411 aptamer, thus affording DSPE-PEG-1411@ICG-J. To fabricate DSPE-PEG-1411@ICG-J/DOX, 0.2 mL of DOX solution (4.0 $mg \cdot mL^{-1}$) and 0.5 mL of DSPE-PEG-1411@ICG-J solution (1.5 $mg \cdot mL^{-1}$) was mixed and shaken at 37 ℃ for 12 h. The product was purified by ultrafiltration and stored at -4 ℃ for further use.

Determination of the grafting efficiency of AS1411 aptamer and DOX loading efficiency on DSPE-PEG-1411@ICG-J/DOX. The grafting efficiency of AS1411 aptamer was quantitatively analyzed by fluorescence spectrophotometry. Therefore, Cy3-labelled aptamer sequence, Cy3-AS1411-COOH, was used to replace AS1411-COOH to proceed the graft reaction. The unreacted DNA sequences in the filtrate were collected after the ultrafiltration, whose fluorescence was measured and amount was quantified according to the fluorescence calibration curve of Cy3-AS1411-COOH (λ_{em} = 500 nm and λ_{ex} = 565 nm) (Figure S18A). Finally, the unreacted DNA amount was subtracted from the total amount of DNA in the reaction to calculate the DNA grafting amount. The final result was the average of three independent measurements.

The DOX loading efficiency was also determined by fluorescence spectrophotometry. The amount of unloaded DOX in the filtrate was quantified by the fluorescence calibration curve of DOX (λ_{em} = 595 nm and λ_{ex} = 488 nm) (Figure S18B), which was subtracted from the total amount of DOX to calculate the DOX loading amount on DSPE-PEG-1411@ICG-J. The final result was the average of three independent measurements.

The DNA sequences used in this work (from 5′ to 3′). AS1411-COOH: HOOC-3[$(CH_2$-$CH_2O)_6$]-GGT GGT GGT GGT TGT GGT GGT GGT GG. Cy3-AS1411-COOH: HOOC-3[$(CH_2$-$CH_2O)_6$]-GGT GGT GGT GGT TGT GGT GGT GGT GG-Cy3.

***In vitro* DOX release profile from DSPE-PEG-1411@ICG-J/DOX.** Two identical solutions of DSPE-PEG-1411@ICG-J/DOX (1.0 mL each, ICG concentration equivalent to 150.0 μg·mL^{-1}) were dialyzed against PBS buffer (10.0 mL, 10.0 mM, pH 7.4) and HAc-NaAc buffer (10.0 mL, 10.0 mM, pH 5.5) at 37 ℃, respectively. At appropriate time points, the old dialysis buffers were replaced by the new one, and the old buffers were collected and the released DOX was quantified according to the fluorescence calibration curve of DOX (λ_{em} = 595 nm and λ_{ex} = 488 nm) (Figure S18B and S18C). The detection continued for 72 h, and the cumulative DOX release at a certain time point can be determined by the following equation:

$$A_T = \frac{\sum_{i=1}^{T} C_i \times 0.01(\mathrm{L})}{90.0\ \mu\mathrm{g}} \times 100\ \%$$

Where A_T stands for the cumulative DOX release at a certain time point; T stands for certain time point; C_i stands for the DOX concentration in the dialysis buffer which was collected at different time points (μg·L^{-1}); 90.0 μg was the total amount of DOX loaded on DSPE-PEG-1411@ICG-J/DOX.

Photothermal conversion efficiency and photostability determination. To determine the photothermal conversion efficiency, in a cuvette an aqueous solution of a sample (1.0 mL) with a certain ICG concentration was continuously irradiated for 500 s with an 880-nm laser at a power of 0.8 W·cm^{-2} (1 cm beam diameter), and the temperature was recorded every 10 s by a digital thermometer. Notably the sample of free ICG (50.0 μg·mL^{-1}) was irradiated with an 808-nm laser

(0.8 $W \cdot cm^{-2}$) according to its optimal absorption. Samples of pure water under the irradiation of 808- and 880-nm laser (0.8 $W \cdot cm^{-2}$) were detected as controls.

For photostability study, the temperatures of the aqueous solutions of various samples (ICG concentration equivalent to 50.0 $\mu g \cdot mL^{-1}$) were recorded every 10 s during five circles of 10-min with irradiation (heating) and 20-min without irradiation (cooling) processes, where the complex micelles based on ICG J-aggregate and free ICG were irradiated by 880- and 808-nm laser (0.8 $W \cdot cm^{-2}$), respectively, according to their maximal absorptions. The absorption spectra and photos of the solutions of free ICG and DSPE-PEG@ICG-J before and after the first test circle were recorded.

Cell culture. A549 and L02 cells were respectively maintained as monolayer cultures in DMEM and PRMI 1640 medium at 37 ℃ in an INCO2/153 CO_2 incubator (Memmert, Germany; 5% CO_2), both of the mediums were supplemented with 10% FBS and 1% penicillin/streptomycin. The cells were cultured until confluence was reached before each experiment.

Animal model. All animal experiments were in accord with Institutional Animal Use and Care Regulations, according to protocol No. SUSTC-JY2017078, approved by the Laboratory Animal Ethics Committee of the Southern University of Science and Technology. After being acclimated and tested for infectious diseases for 1 week, 4-week-old BALB/c nude mice were subcutaneously injected with A549 cells (1×10^7 cells each mouse) at the flank region. After about two weeks, mice with tumor volumes of about 80-150 mm^3 were randomized into treatment groups. The tumor size was calculated using the following formula: Volume = (Length $\times$ $Width^2$)/2.

***In vitro* and *in vivo* biostability determination.** First, 10% FBS was utilized to mimic the biological environment. Samples were dispersed in 10% FBS to form suspensions with ICG

concentrations equivalent to 10.0 μg·mL^{-1}, which were shaken at 37 ℃ for 24 h; the absorption spectra of the final samples were detected. To determine the biostability for intracellular application, samples were dispersed in basic DMEM to form suspensions with ICG concentrations equivalent to 10.0 μg·mL^{-1}, which were incubated with A549 cells (in the logarithmic growth phase) for 12 h at 37 ℃, thereafter, the cells were washed three times with PBS buffer, further digested with 0.25% (w/v) trypsin-0.03% (w/v) EDTA solution; The collected cells were centrifuged and re-suspended in PBS buffer (0.5 mL) for absorption spectra test. For *in vivo* biostability determination, samples (150.0 μL) with ICG concentrations equivalent to 0.5 mg·mL^{-1} were intravenously injected to BALB/c nude mice, and then the *in vivo* fluorescence images were obtained at different time points after the injection *via* the animal fluorescence imaging system.

Cellular uptake study. Free ICG, DSPE-PEG@ICG-J, DSPE-PEG-1411@ICG-J and DSPE-PEG-1411@ICG-J/DOX were dispersed in the basic DMEM (ICG concentration equivalent to 25.0 μg·mL^{-1}) and incubated with A549 cells in 6-well plates for 4 h at 37 ℃, the un-internalized samples were removed, thereafter, the cells were washed three times with PBS buffer, further digested with 0.25% (w/v) trypsin-0.03% (w/v) EDTA solution; The collected cells were centrifuged, and re-suspended in PBS buffer (1.0 mL) for cell counting. Next, the cells were centrifuged again and re-suspended in a mixed solvent of DMSO and H_2O (v/v = 4/1, and 1.0 mL total volume), and disrupted by an ultrasonic cell disruptor. Due to the presence of DMSO and the ultrasonic treatment, the micelles disassembled and ICG J-aggregates broke up to free ICG. Therefore, the cellular uptake amount of ICG was evaluated by the absorption calibration curve of free ICG (Figure S18D).

Cytotoxicity and *in vitro* anti-cancer therapy. To detect the dark cytotoxicity, A549 and L02 cells were seeded in 96-well plates and pre-cultured for 24 h, and then the mediums were replaced

by 90.0 μL of fresh medium along with 10.0 μL of sample suspension in PBS buffer with ICG concentrations equivalent to 0.0, 5.0, 10.0, 25.0, 50.0, 75.0 and 100.0 $\mu g \cdot mL^{-1}$. After a 4-h incubation, the cells were gently washed by PBS buffer for three times to remove the non-internalized samples, thereafter, the cells were cultured for another 24 h (37 ℃, 5% CO_2). The cell viabilities were determined by MTT assay, and the results were presented as average ± SD (n = 5).

For *in vitro* anti-cancer therapy study, A549 cells were seeded in 96-well plates and pre-cultured for 24 h, and then the mediums were replaced by 90.0 μL of fresh mediums along with 10.0 μL of sample suspension in PBS buffer with ICG concentrations equivalent to 0.0, 5.0, 10.0, 25.0, 50.0, 75.0 and 100.0 $\mu g \cdot mL^{-1}$. After 4-h incubation, the cells were gently washed by PBS buffer for three times to remove the non-internalized samples; Next, the cells were applied to laser irradiation (0.8 $W \cdot cm^{-2}$) for 10 min (Notably, 808 nm-laser for ICG and 880-nm laser for the micelle samples based on ICG J-aggregate), and then the cells were further cultured for 24 h (37 ℃, 5% CO_2). Finally, the cell viabilities were determined by MTT assay, and the results were presented as average ± SD (n = 5).

***In vitro* and *in vivo* photoacoustic imaging.** For in vitro photoacoustic tests, a cuboid container was filled with 2.0% agarose gel to half depth. Aqueous solutions of various samples (with different ICG equivalent concentrations ranging from 20.0 to 100.0 $\mu g \cdot mL^{-1}$) were filled into polyethylene capillaries, consequently, which were laid on the surface of the solidified agarose gel and further covered with thin 2.0% agarose gel to make the surface smooth.

For *in vivo* photoacoustic imaging, the aqueous solutions (150.0 μL) of various samples with an ICG concentration equivalent to 0.5 $mg \cdot mL^{-1}$ were intravenously injected to the mice. The PAI images were collected at different time points after the injection.

Blood circulation analysis and bio-distribution measurement. For the blood circulation analysis, three SD rats were administered with DSPE-PEG-1411@ICG-J/DOX at an ICG equivalent dose of 4 mg kg^{-1}. After predetermined time intervals (15 and 30 min; 1, 2, 4, 8, 12, 24, and 48 h), blood was taken from tail artery of SD rats and stored in heparinized tubes. To each blood sample (50 μL), 200 μL DMSO was added to convert the ICG J-aggregates in DSPE-PEG-1411@ICG-J/DOX to free ICG. The amount of ICG were measured by HPLC along with the absorption calibration curve of ICG (Figure S18E), and normalized to percentages of injected dose per gram of blood (% ID g^{-1}). A first order exponential decay was fitted to the data, giving an accurate model of the DSPE-PEG-1411@ICG-J/DOX blood clearance time. For the bio-distribution measurement, sample suspensions (150.0 μL) with an ICG concentration equivalent to 0.5 mg·mL^{-1} were injected into the A549 tumor-bearing mice *via* the tail vein. The mice were sacrificed 12 h after the injection (n = 3 for each group), and their tumors, livers, spleens, kidneys, lungs, and hearts were excised. All these tissues were weighed and homogenized in a cooled glass tissue grinder, and then ICG was extracted from the tissue slurries using a mixed solvent of DMSO and H_2O (v/v = 4/1)**.** Finally, the amount of ICG were measured by HPLC along with the absorption calibration curve of ICG (Figure S18E), and normalized to percentages of injected dose per gram of tissue (% ID g^{-1}).

HPLC quantification method: Flow rates were 0.5 mL·min^{-1}. Injection volumes were 50.0 μL. The column temperature was maintained at 40 ℃ throughout the analysis. UV absorbance was monitored at 780 nm. The gradient solvent system was TEAA (100.0 mM, pH 7.0)/acetonitrile. The percentage of acetonitrile linearly increased from 5% to 100% within the 20 min analysis period.

***In vivo* anticancer therapy.** The A549 tumor-bearing mice were randomly divided into 9 groups consisting of 4 mice in each group. The untreated mice in group i was used as a control. 150.0 μL of DOX in PBS buffer (0.3 $mg \cdot mL^{-1}$), PBS buffer, free ICG in PBS buffer (0.5 $mg \cdot mL^{-1}$) were injected sequentially to the mice *via* the tail vein, which were denoted as group ii to iv; 150.0 μL of DSPE-PEG@ICG-J and DSPE-PEG-1411@ICG-J in PBS buffer (ICG concentration equivalent to 0.5 $mg \cdot mL^{-1}$) were injected sequentially to the mice *via* the tail vein, respectively, which were denoted as group vii and viii. For the mice in both group vi and ix, 150.0 μL of DSPE-PEG-1411@ICG-J/DOX (ICG concentration equivalent to 0.5 $mg \cdot mL^{-1}$) were intravenously injected. 1 h after the injection, the mice in group iv were irradiated at their tumor sites by a 808-nm laser for 10 min (0.8 $W \cdot cm^{-2}$); 12 h after the injection, the mice in group iii, vii, viii, and ix were irradiated at their tumor sites by a 880-nm laser for 10 min (0.8 $W \cdot cm^{-2}$); no irradiation was applied to the mice in group i, ii, and vi. 12 h after the treatments, one mouse in each group was sacrificed by cervical dislocation for necropsy, and its tumor was collected for tissue slicing and staining. For the left mice, their tumor sizes were measured by utilizing a caliper every 2 days for a period of 24 days, and the tumor volumes were calculated using the following formula: Volume = $(\text{Length} \times \text{Width}^2)/2$. After the 24-day treatment, the mice in group ix were sacrificed by cervical dislocation for necropsy, their major organs including hearts, livers, spleens, lungs, and kidneys were harvested for tissue slicing and staining. For the mice in group v, 150.0 μL of Doxil in PBS buffer (DOX concentration equivalent to 0.3 $mg \cdot mL^{-1}$) was intravenously injected every 4 days for 3 times in total, and the day for conducting the first injection was designated as day 1. 12 h after the first treatment, one mouse was sacrificed by cervical dislocation for necropsy, and its tumor was collected for tissue slicing and staining. For the left mice, the tumor size measurement and tumor volume calculation were conducted according to the same method of other groups.

H&E staining. The tissues were fixed in 10 % neutral buffered formalin, processed routinely into paraffin, sectioned at 4 μm, stained with hematoxylin-eosin (H&E) and examined by optical microscope.

SUPPLEMENTAL TABLE

Table S1. Comparison of tissue penetration ability of 808- and 880-nm lasers.[a] Related to Scheme 1, and Figure 3 and 4.

Remaining Power (%)		
Pork slide thickness (mm)	808-nm laser	880-nm laser
0.5	35.25 ± 1.1	57.75 ± 0.3
1.0	19.18 ± 0.9	35.47 ± 0.9
1.5	13.37 ± 0.5	22.88 ± 1.2

[a] We measured the percentage of the remaining power of a beam from 808- or 880-nm laser (0.8 W cm^{-2}) after it penetrated the pork slides with different thicknesses.

SUPPLEMENTAL FIGURES

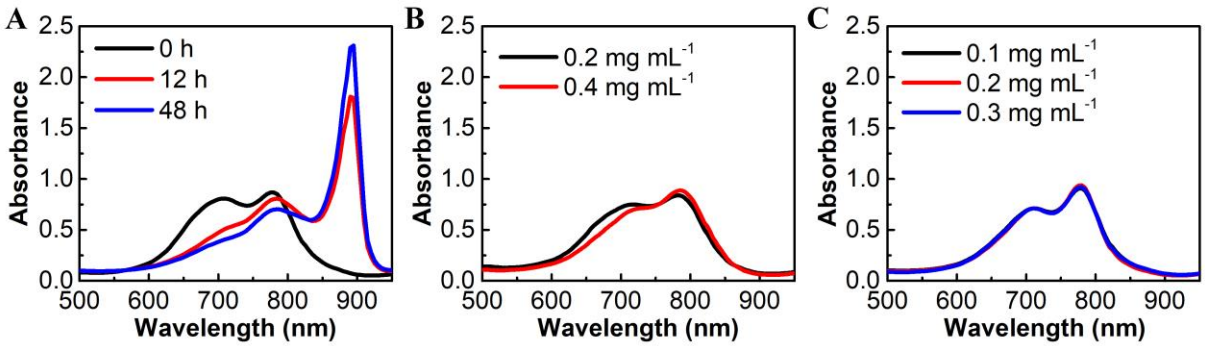

Figure S1. Monitoring ICG aggregation under different conditions via absorption spectrum. (A) In the presence of DSPE-PEG_{2k}-NH_2 (0.2 $mg \cdot mL^{-1}$) with room-temperature stirring in water. (B and C) Mixing with different concentrations of (B) DSPE-PEG_{2k} and (C) PEG_{2k}-NH_2 in water after 24 h of stirring at room temperature. In all the experiments, the concentration of ICG was 50.0 μg mL^{-1}. Related to Figure 1.

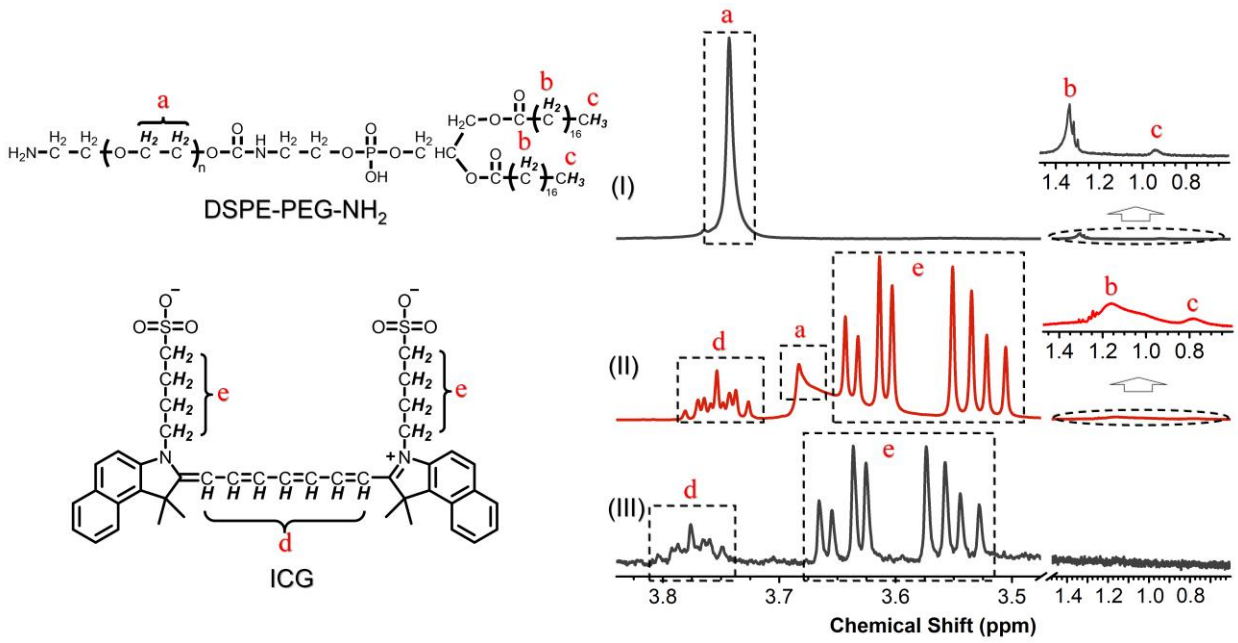

Figure S2. ^1H NMR spectra of (I) DSPE-PEG_{2k}-NH_2 micelle, (II) DSPE-PEG_{2k}-NH_2 micelle with ICG J-aggregate in encapsulation, and (III) naked ICG J-aggregate, as well as the assignment of the peaks. Related to Figure 1.

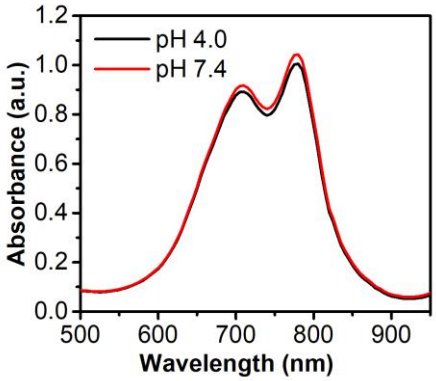

Figure S3. The absorption spectra of ICG (10.0 mg mL^{-1}, PBS buffers of pH 4.0 and 7.4) after a 24-h stirring at room temperature. The solutions were diluted with corresponding buffer before the tests. Related to Figure 1.

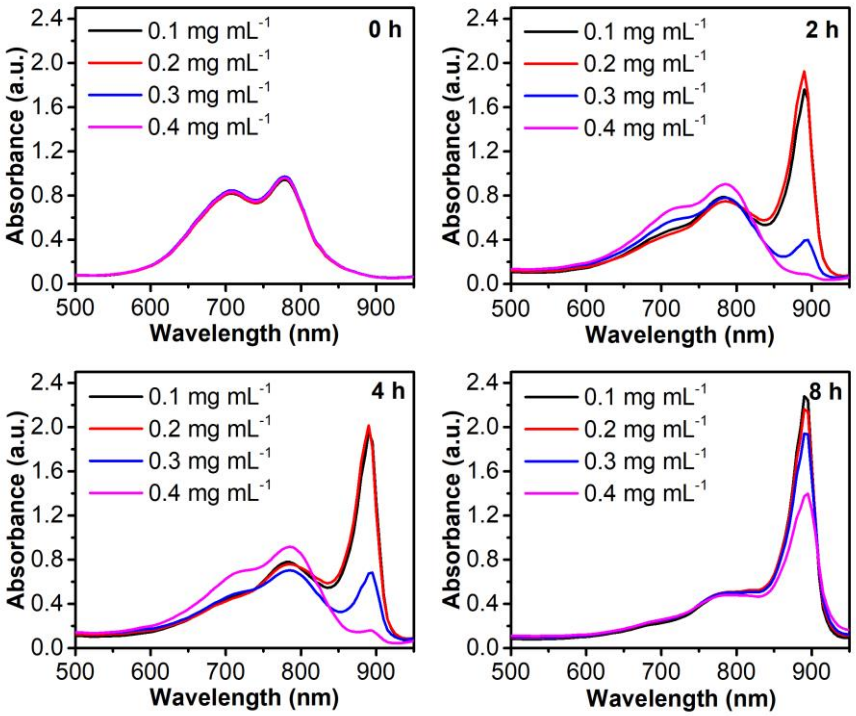

Figure S4. The absorption spectra of the aqueous mixtures between ICG (50.0 μg mL^{-1}) and different concentrations of DSPE-PEG_{2k}-NH_2. The mixtures were first heated at 80 °C for 15 min,

thereafter their absorption spectra were detected at different time points during the subsequent stirring process. Related to Figure 2.

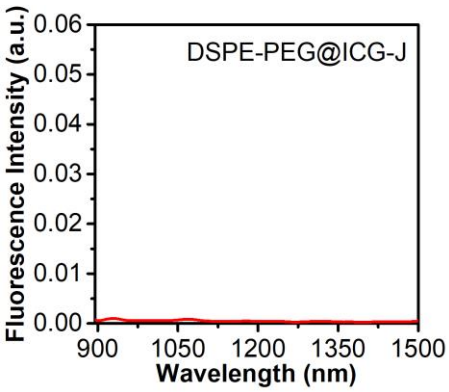

Figure S5. The fluorescence spectrum of DSPE-PEG@ICG-J, which was excited at wavelength of 880 nm. Related to Figure 2.

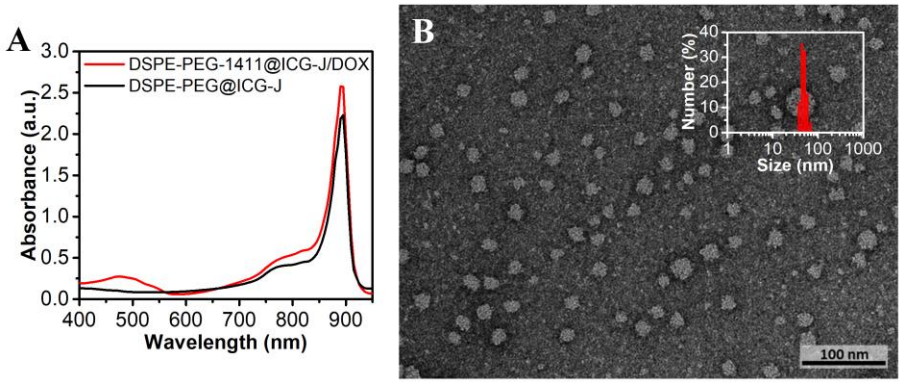

Figure S6. (A) The absorption spectrum of DSPE-PEG-1411@ICG-J/DOX (the red line), in which a typical peak at 480 nm was additionally observed as compared with the absorption of DSPE-PEG@ICG-J (the black line), indicating that DOX has been successfully loaded to the micelles.

(B) The TEM image and DLS characterization result (inset) of DSPE-PEG-1411@ICG-J/DOX. Related to Figure 3 and 4.

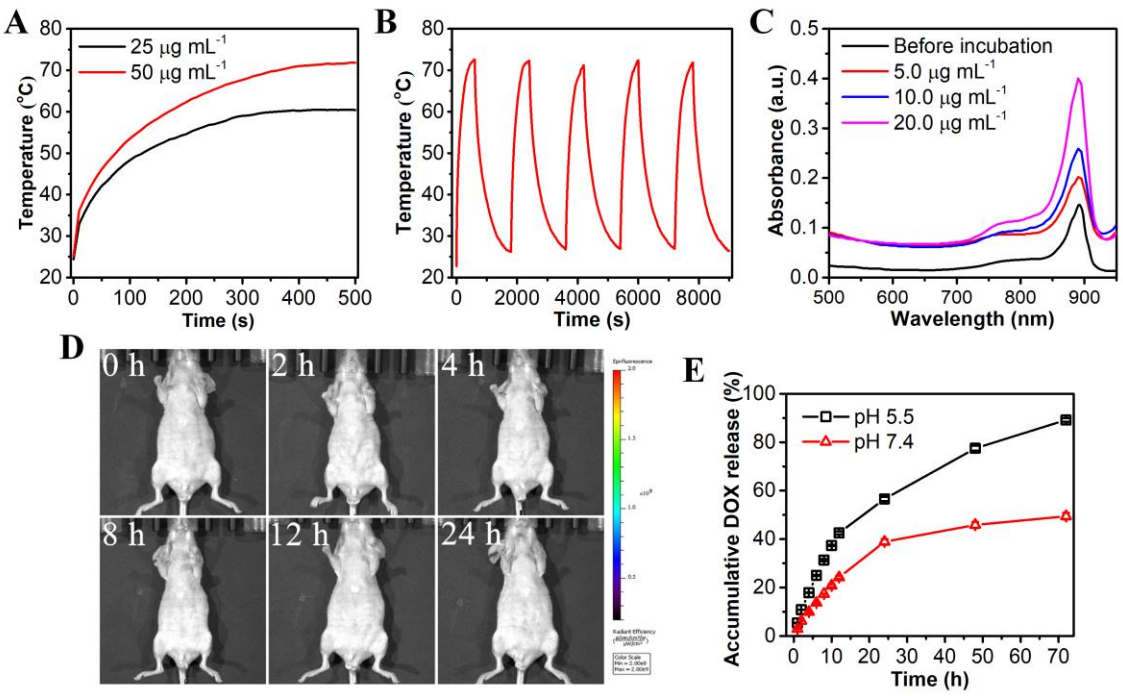

Figure S7. Detection of the photothermal conversion efficiency, the stability, and the drug release profiles of DSPE-PEG-1411@ICG-J/DOX. (A) The photothermal heating curves of DSPE-PEG-1411@ICG-J/DOX solution at different concentrations under 880-nm laser irradiation at a power density of 0.8 W cm^{-2} for 500 s. (B) Temperature change of DSPE-PEG-1411@ICG-J/DOX solution (ICG concentration equivalent to 50.0 μg mL^{-1}) recorded every 10 s during five circles of 10-min with irradiation (heating) and 20-min without irradiation (cooling) processes. (C) The absorption spectra of the suspensions of A549 cells incubated with DSPE-PEG-1411@ICG-J/DOX at different concentration for 4-h. (D) The fluorescence images obtained by the animal fluorescence imaging system at different time points after 150.0 μL of DSPE-PEG-1411@ICG-J/DOX solution (ICG concentration equvalent to 0.5 mg mL^{-1}) was intravenously injected to BALB/c nude mice. (E) *In vitro* DOX-release profiles of DSPE-PEG-1411@ICG-J/DOX in PBS

buffer (pH 7.4) and HAc-NaAc buffer (pH 5.5). Error bars indicate standard errors of triplicate tests. Related to Figure 3 and 4.

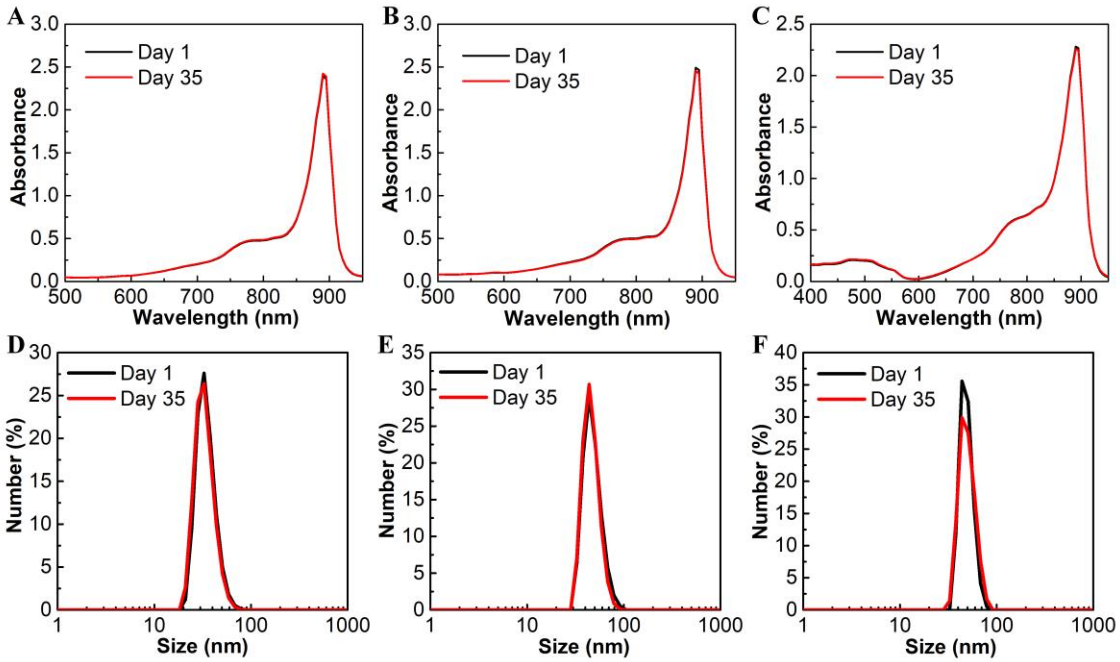

Figure S8. The absorption spectra and DLS analysis results of (A, D) DSPE-PEG@ICG-J, (B, E) DSPE-PEG-1411@ICG-J, and (C, F) DSPE-PEG-1411@ICG-J/DOX at the first day (Day 1) and last day (Day 35) of the long-term stability detection. Related to Figure 3 and 4.

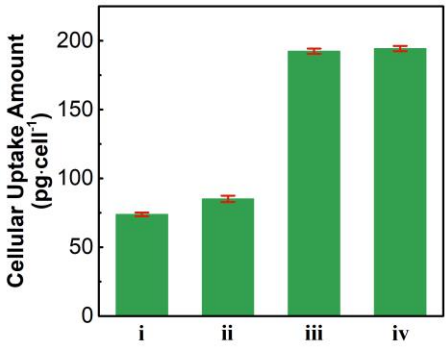

Figure S9. The cellular uptake results of i) ICG, ii) DSPE-PEG@ICG-J, iii) DSPE-PEG-1411@ICG-J, and iv) DSPE-PEG-1411@ICG-J/DOX in live A549 cells after 4-h incubation. For all the samples, ICG concentration equivalent to 25.0 μg·mL^{-1}. Data are presented as the average ± SD (n = 3). Related to Figure 4.

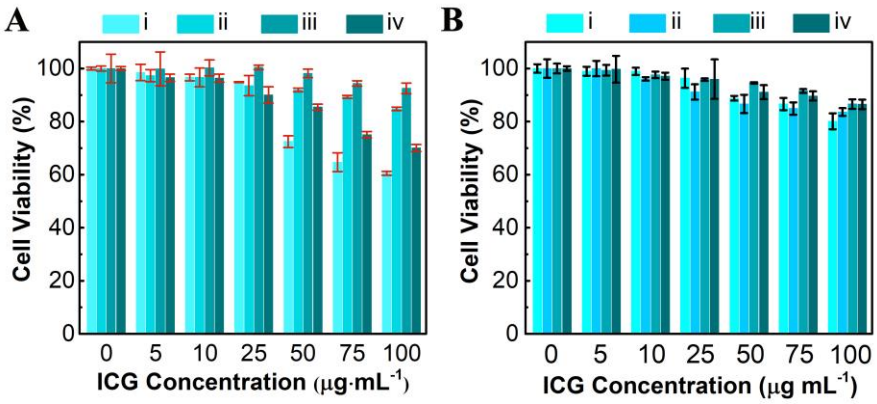

Figure S10. The dark cytotoxicity of i) ICG, ii) DSPE-PEG@ICG-J, iii) DSPE-PEG-1411@ICG-J, and iv) DSPE-PEG-1411@ICG-J/DOX to (A) A549 and (B) normal L02 cells determined by MTT assay. Error bars indicate standard errors of quintuple tests. Related to Figure 4.

The dark cytotoxicities of DSPE-PEG@ICG-J, DSPE-PEG-1411@ICG-J, and DSPE-PEG-1411@ICG-J/DOX were tested on A549 and normal human hepatic L02 cell lines by MTT assay to evaluate their biocompatibilities at the cellular level, where free ICG was used as a comparison. At concentrations larger than 50 μg·mL^{-1}, the free ICG started to show cytotoxicity, while the complex micelles loaded with equivalent amounts of ICG showed negligible cytotoxicity (Figure S9). The results demonstrated that the biocompatibility of ICG has been further improved through DSPE-PEG encapsulation. In addition, AS1411 conjugation did not bring any side effect to the

complex micelle. DSPE-PEG-1411@ICG-J/DOX did show some cytotoxicity at high concentrations, which should be caused by the intrinsic toxicity of DOX.

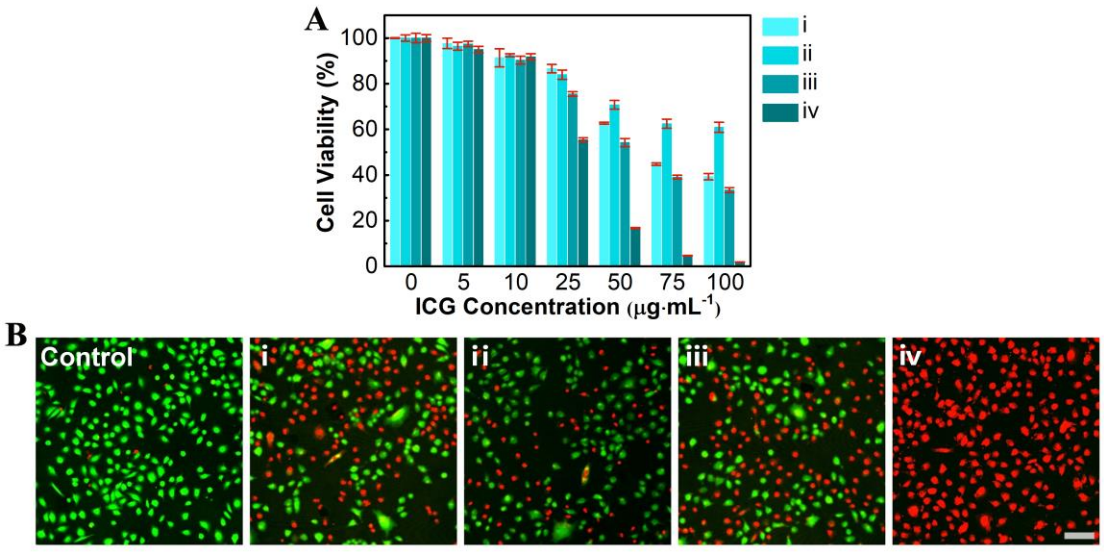

Figure S11. The *in vitro* anticancer therapy study result. Sample: i) ICG; ii) DSPE-PEG@ICG-J; iii) DSPE-PEG-1411@ICG-J; iv) DSPE-PEG-1411@ICG-J/DOX. (A) Viability of A549 cells following PTT with various samples for 10 min laser irradiation (0.8 W cm^{-2}, 808-nm laser for ICG, and 880-nm laser for the micelles); data are presented as the average ± SD (n = 5). (B) Fluorescence images of Calcein AM/PI stained A549 cells incubated with various samples (ICG concentration equivalent to 100 μg·mL^{-1}) after PTT. The scale bar is 100 μm. Related to Figure 4.

In the *in vitro* anticancer therapy study, in order to clarify the role of each component in the final complex micelle, DSPE-PEG@ICG-J, DSPE-PEG-1411@ICG-J, and DSPE-PEG-1411@ICG-J/DOX were systematically investigated to elucidate the PTT effect of ICG J-aggregates, the targeting effect of AS1411, and the chemotherapy effect of DOX. In detail, the samples (the amounts were normalized by ICG concentration) were incubated with A549 cells for

4 h, thoroughly washed by PBS, and then irradiated by laser at a power density of 0.8 $W \cdot cm^{-2}$ for 10 min; finally, the cell viability was evaluated by MTT assay after an additional 24-h culture. Notably, lasers at different wavelengths were selected to match the optimal absorptions of free ICG (808 nm) and ICG J-aggregate (880 nm). As shown in Figure S10A, from an ICG equivalent concentration of 50 $\mu g \cdot mL^{-1}$, free ICG and DSPE-PEG@ICG-J started to show visible cytotoxicity. The group of free ICG showed higher cytotoxicity compared with the group of DSPE-PEG@ICG-J, which mainly came from the intrinsic cytotoxicity of ICG at high concentrations according to the results of dark cytotoxicity test. On the other hand, after irradiation, the cytotoxicity of DSPE-PEG@ICG-J increased with respect to that under dark condition, which demonstrated the toxic PTT effect of ICG J-aggregate. After the integration of AS1411 aptamer, significantly intensified cytotoxicity was observed from DSPE-PEG-1411@ICG-J, indicating that a 2.6-fold improvement in cellular uptake by the presence of AS1411 greatly facilitated the PTT effect of the complex micelles. Finally, DSPE-PEG-1411@ICG-J/DOX which integrated with three functionalities could kill 99.2% cells at an ICG equivalent concentration of 100 $\mu g \cdot mL^{-1}$. This cell-killing rate was much better than those in the PTT dominant group (DSPE-PEG-1411@ICG-J with irradiation) and the chemotherapy dominant group (DSPE-PEG-1411@ICG-J/DOX without irradiation). Therefore, we concluded that the remarkably enhanced anticancer efficacy of DSPE-PEG-1411@ICG-J/DOX under laser irradiation derived from the synergistic interaction between chemotherapy and PTT; the similar synergistic effect has been observed in many other related studies and considered as an efficient anticancer strategy (Yan et al., 2018; Zhang et al., 2018; Wang et al., 2018; Xu et al., 2019). To further visualize the cancer cell killing effect contributed from PTT, targeting, and chemotherapy, the above cells treated with free ICG and micelles (ICG equivalent concentration at 100 $\mu g \cdot mL^{-1}$) were stained with calcein acetoxymethyl ester (Calcein-

AM) and propidium iodide (PI) to identify live and dead/late apoptotic cells (Figure S10B). The result was inconsistent with the MTT assay result, indicating the remarkable anticancer efficacy of DSPE-PEG-1411@ICG-J/DOX through synergistic enhancement of its respective components.

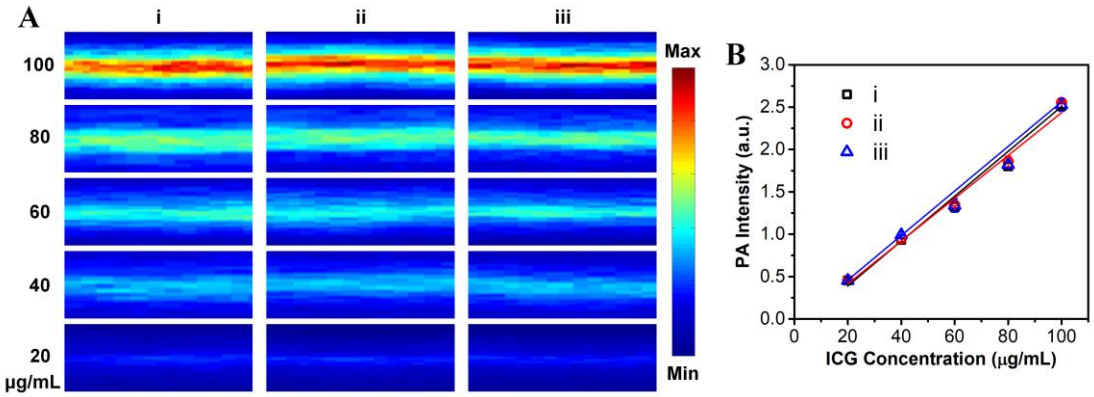

Figure S12. *In vitro* determination of the photoacoustic properties of i) DSPE-PEG@ICG-J, ii) DSPE-PEG-1411@ICG-J, and iii) DSPE-PEG-1411@ICG-J/DOX. (A) The PA images of the micelles upon excitation at 880 nm (pulsed laser) at different ICG equivalent concentrations. (B) PA intensities of the micelles at 880 nm as a function of ICG equivalent concentrations. Related to Figure 3.

Since the photoacoustic response of the three kinds of complex micelles all comes from the ICG J aggregates encapsulated in them, they displayed consistent photoacoustic signals at the same ICG equivalent concentrations.

The photoacoustic signal intensities of the complex micelles are linearly related to their ICG equivalent concentrations.

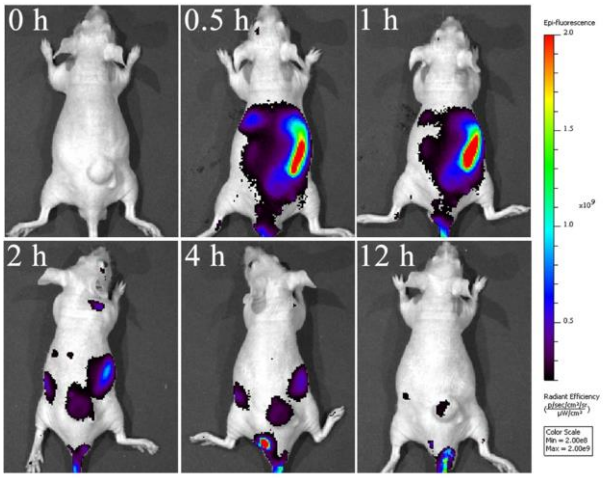

Figure S13. The fluorescence-indicated metabolism of ICG in mouse. The fluorescence images obtained by animal fluorescence imaging system at different time points after 150.0 μL of ICG solution (0.5 mg mL^{-1}) was intravenously injected to the BALB/c nude mice. Related to Figure 3.

The result demonstrated that ICG would reach the maximum accumulation at the tumor-site about 1 h after the intravenous injection.

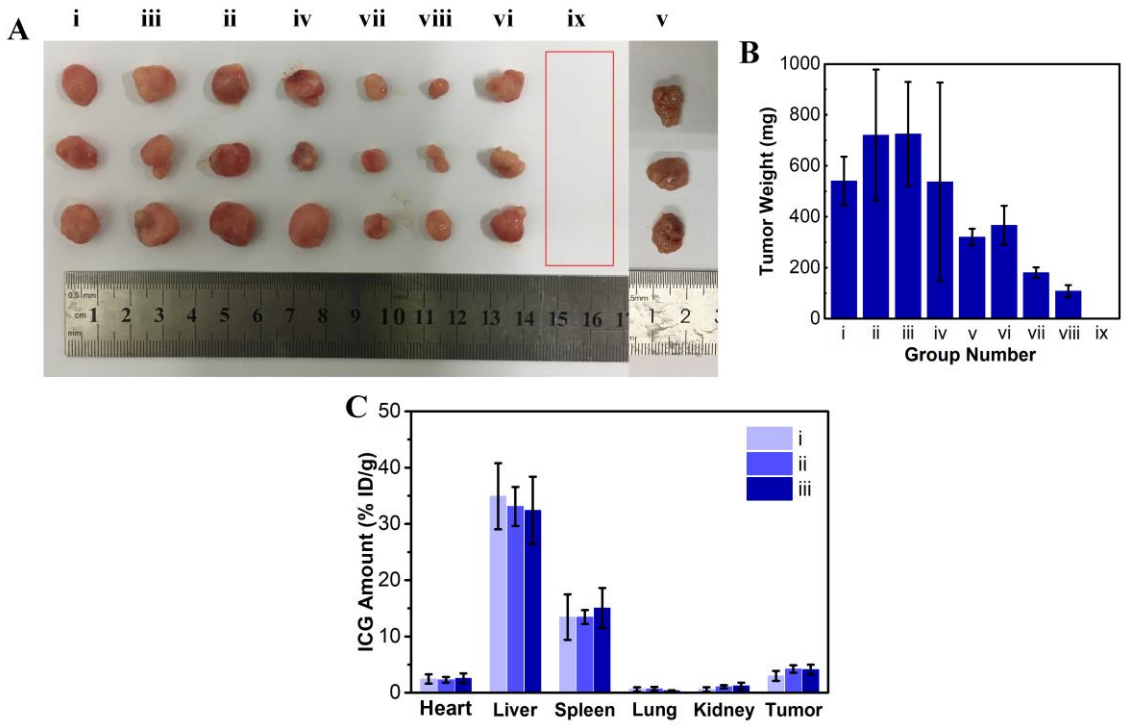

Figure S14. The (A) pictures and (B) weights of the tumors collected 24 days after the treatments: i) Control; ii) DOX; iii) PBS + 880-nm laser; iv) ICG + 808-nm laser; v) Doxil; vi) DSPE-PEG-1411@ICG-J/DOX; vii) DSPE-PEG@ICG-J + 880-nm laser; viii) DSPE-PEG-1411@ICG-J + 880-nm laser; ix) DSPE-PEG-1411@ICG-J/DOX + 880-nm laser. The power density of both 808-nm and 880-nm lasers is 0.8 W cm^{-2}. (C) *Ex vivo* bio-distributions of i) DSPE-PEG@ICG-J, ii) DSPE-PEG-1411@ICG-J, and iii) DSPE-PEG-1411@ICG-J/DOX in the main organs and tumor tissues of mice at 12 h post intravenous administration (n = 3). In the experiment, intravenous injection valume of the samples is 150.0 μL, for ICG and the micelles, ICG concentration equivalent to 0.5 mg·mL^{-1}; for DOX and Doxil, DOX concentration equivalent to 0.3 mg·mL^{-1}. Related to Figure 4.

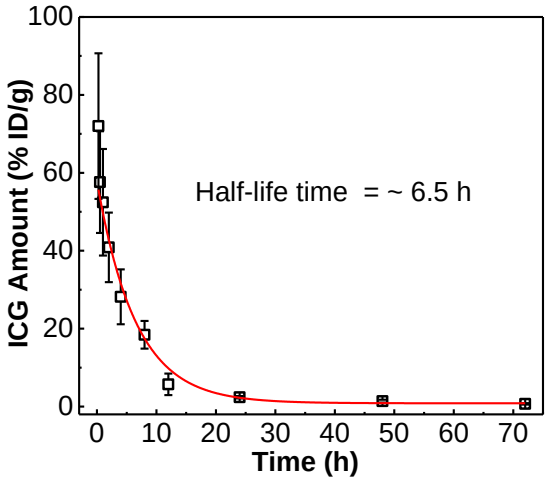

Figure S15. Blood circulation analysis of SD rats intravenously injected with DSPE-PEG-1411@ICG-J/DOX (at ICG equivalent dose of 4 mg kg^{-1}). Related to Figure 4.

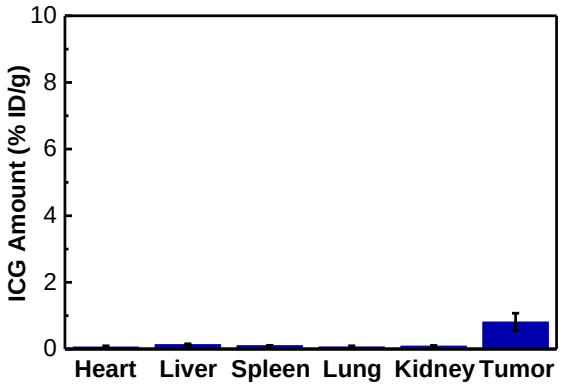

Figure S16. *Ex vivo* bio-distribution of DSPE-PEG-1411@ICG-J/DOX in the main organs and tumor tissues of mice at 7 days post intravenous administration (n = 3). 150 μL of DSPE-PEG-1411@ICG-J/DOX was injected at ICG equivalent concentration of 0.5 mg·mL^{-1}. Related to Figure 4.

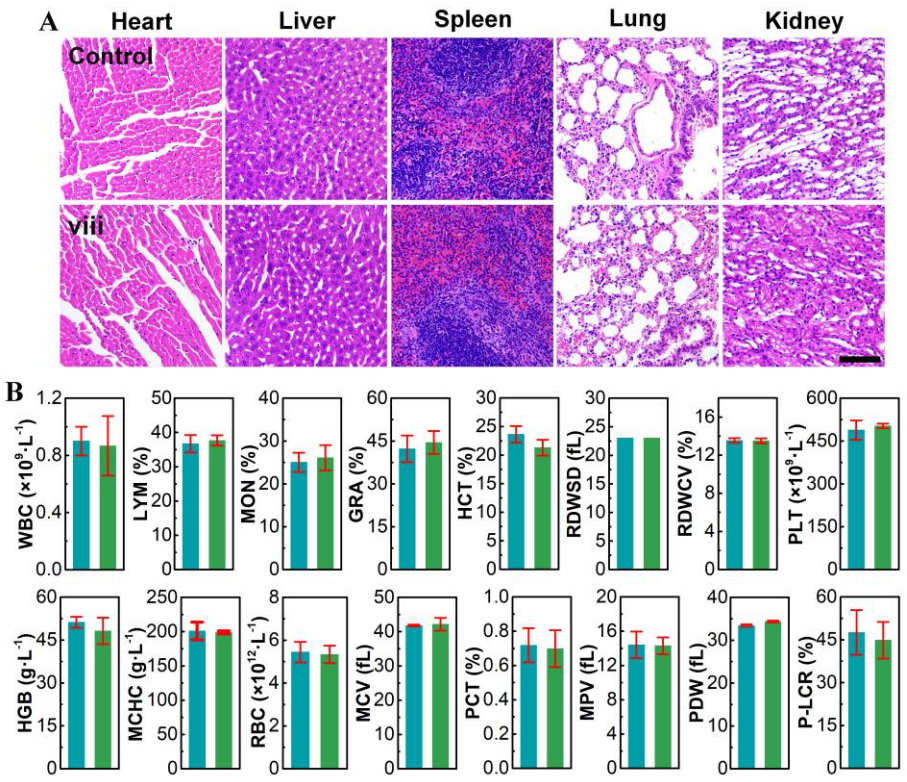

Figure S17. Histology and blood tests of the healed mice in the *in vivo* anticancer therapy study. (A) Histological H&E staining for different organs collected from mice in group ix, and the organs in control group were collected from health mice. The scale bar is 100 μm. (B) Blood tests for healthy mice (blue bars) and the mice in group ix (green bars), data are presented as the average ± SD (n = 3). Related to Figure 4.

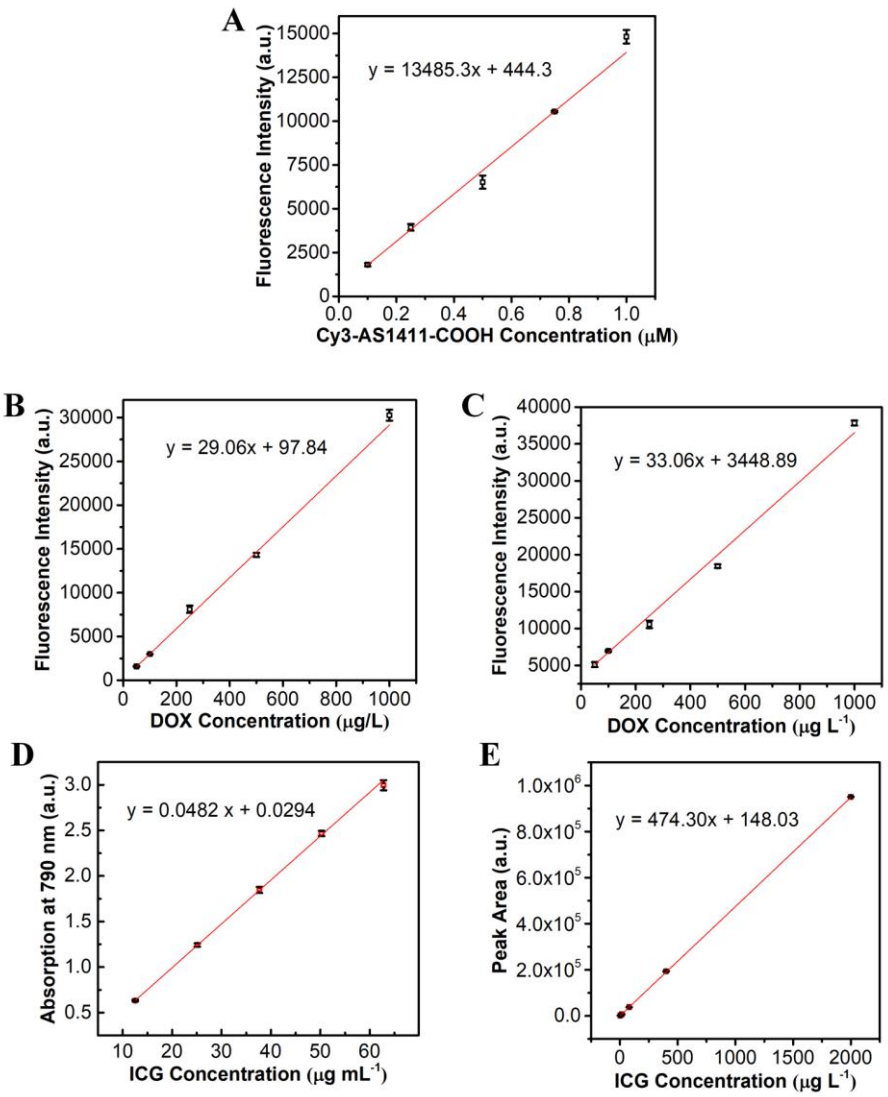

Figure S18. The calibration curves. (A) The fluorescence calibration curve of Cy3-AS1411-COOH, the excitation wavelength was 500 nm, and the emission was measured at wavelength of 565 nm. The fluorescence calibration curve of DOX in (B) PBS (pH 7.4) and (C) HAc-NaAc buffer (pH 5.5), the excitation wavelength was 488 nm, and the emission was measured at the wavelength of 595 nm. (D) The absorption calibration curve of free ICG for the cellular uptake study. (E) The absorption calibration curve of ICG for the bio-distribution study. Related to Figure 3 and 4.

Supplemental References

Yan, G. W., Li, A. H., Zhang, A. T., Sun, Y., and Liu, J. Q. (2018). Polymer-based nanocarriers for co-delivery and combination of diverse therapies against cancers. Nanomaterials *8*, 85.

Zhang, A., Li, A., Zhao, W., and Liu, J. (2018). Recent advances in functional polymer decorated two-dimensional transition-metal dichalcogenides nanomaterials for chemo-photothermal therapy. Chem.-Eur. J. *24*, 4215-4227.

Wang, J., Dong, Y., Li, Y., Li, W., Cheng, K., Qian, Y., Xu, G., Zhang, X., Hu, L., Chen, P., et al. (2018). Designer exosomes for active targeted chemo-photothermal synergistic tumor therapy. Adv. Funct. Mater. *28*, 1707360.

Xu, Y., Chen, J., Tong, L., Su, P., Liu, Y., Gu, B., Bao, B., and Wang, L. (2019). pH/NIR-responsive semiconducting polymer nanoparticles for highly effective photoacoustic image guided chemo-photothermal synergistic therapy. J. Control. Release *293*, 94-103.